Unknots, knots, links and necklaces made of dislocations in cholesterics

P Pieranski, M H Godinho

RESEARCH ARTICLE

Unknots, knots, links and necklaces made of dislocations in cholesterics

P. Pieranski[a] and M.H. Godinho[b]

[a]Laboratoire de Physique des Solides, Université Paris-Saclay, Orsay, France;
[b]i3N/CENIMAT, Department of Materials Science, NOVA School of Science and Technology, NOVA University Lisbon, Campus de Caparica, Caparica 2829-516, Portugal

ARTICLE HISTORY
Compiled June 27, 2024

ABSTRACT
We deal with the genesis and decay of knots and links made of dislocations in a cholesteric layer confined in the gap between orthogonal cylindrical mica sheets. The genesis starts by nucleation of folded unknots driven by a compressive strain. The nucleation process of the trivial and folded unknots is studied and discussed in detail. We show that the expansion of the folded unknots leads to their lateral collisions followed by the coalescence into the torus knots, such as the trefoil knot, or into the links, such as the Hopf and Solomon links. The viscoelastic decays of knots and links follow well defined pathes involving topological and geometrical transformations. In particular, the symmetric configuration of the Hopf link is unstable with respect to the shrinking of one of its interlaced loops. The final asymmetric configuration, made of a minimal loop tethered on a large cargo loop, is called the Hopf necklace. Similarly, the double Hopf necklace is obtained by the elastic decay of the Solomon link. We emphasize that Hopf necklaces of various orders are quite ubiquitous.

KEYWORDS
unknots, knots, links, necklaces, dislocations, cholesterics, topological defects

1. Introduction

1.1. Objects with a double topological character

Linear topological defects such dislocations or disclinations occur in systems with order parameters resulting from broken symmetries [1,2]. For topological reasons, they must either end on surfaces or to form closed loops. For mathematicians, closed dislocation or disclination loops look like closed one dimensional lines embedded in a three dimensional space. Therefore, from this abstract point of view, they must be equivalent to unknots or to form knots or links.

After the discovery of the Hopf link (called in French "double anneau", see Figure 1f) made of dislocations in cholesterics by Bouligand [3], Bouligand et al. [4] stressed for the first time that we have to deal with objects having a double topological character.

Subsequently, Tkalec et al. [5] pointed out that all kinds of knots and links can be generated in a controlled manner from disclinations of rank $m = 1/2$ in a suspension of colloidal microspheres in chiral nematics. Using free energy minimization, Seč et al.

CONTACT P. Pieranski. Email: pawel.pieranski@u-psud.fr

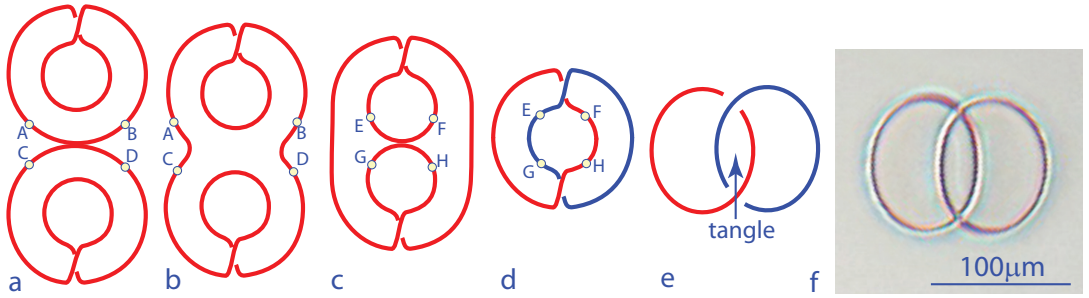

Figure 1. The "double anneaux" Hopf link made of dislocation loops in cholesterics [3,4]. a) Two unknots folded once. a-b) By the coalescence-rewiring of the external segments, $AB + CD \Rightarrow AC + BD$, one obtains an unknot with two folds. c-e) By the coalescence-rewiring of the two folds, $EF + GH \Rightarrow EG + FH$, one obtains the Hopf link made of two interlaced loops. f) The Hopf link generated by the coalescence method in experiments reported in section 9.2 (5CB/CB15 mixture).

[6] explored a large variety of knots or links made of $m = 1/2$ disclinations confined is cholesteric droplets. An exhaustive review of his own and other contributions to the field of knots and links in liquid crystals was published in 2020 by Smalyukh [7].

Our former studies of knots [8] and tangles [9] made of dislocations in cholesterics added a new contribution to this field. Recently, we have succeeded in producing torus knots and links by coalescence of the folded unknots mentioned for the first time in ref. [8]. As an example we show in Figure 1 that coalescence of two unknots folded once produces the Bouligand's "double anneau" configuration of two interlaced dislocation loops i.e. the Hopf link.

1.2. Content of this article

This paper is organized as follows:

(1) In section 2, for historical reason, we discuss first the emission of disclination loops in nematics, conjectured in 1969 by Friedel and de Gennes [10], which is closely related to the nucleation of dislocation loops in cholesterics. We stress that this conjecture was proved recently to be true by Long et al. [11] who reported on the Frank-Reed mechanism of nucleation of disclination loops on pairs of $\pm 1/2$ anchoring defects.
(2) As the genesis of knots and links made of dislocations in cholesterics starts by nucleation of the folded dislocation loops (folded unknots), in section 3 we extend the Friedel-de Gennes conjucture to the principle of the emission of the trivial and folded dislocations loops.
(3) In section 4, we describe the setup and methods used in our experiments.
(4) For the sake of clarity, using as an example systems of concentric dislocation loops generated by the confinement inside the gap between the crossed cylindrical mica sheets, we remind in section 5 the structures of dislocations called simple and double characterised respectively by Burgers vectors $b = p/2$ and $b = p$ (defined for the first time by Kleman and Friedel [12]).
(5) Even if knots and links are made of the double dislocations, in section 6 we report, for the sake of completeness, first on nucleation of individual simple dislocation loops which are similar to disclinations in nematics. This nucleation is driven by

a large enough compression of the cylinder/cylinder gap thickness measured by the Compression Ratio defined as $CR = p_o/p$ where p_o is the natural cholesteric pitch and p is the reduced pitch due to the compressive strain.

(6) Experiments on nucleation of the double dislocation loops (trivial and folded) are reported in section 7. We show that the Critical Compression Ratio necessary for nucleation scales with the size D_{def} as as $(D_{def}/p_o)^{-1}$.

(7) For interpretation of this last result, we will transpose in section 8 the nucleation model proposed by Zappone and Bartolino [13] to a dimensionless form and use also results of the recent work of Long et al. [11]. We also discuss nucleation of the folded dislocation loops.

(8) In section 9, we report on the genesis of links and knots by coalescence of unknots folded once or twice.

(9) In the next section 10, we analyse first the stability of the crossing in knots and links and we report on the decay process *trefoil knot* $\Rightarrow$ *simple Hopf necklace* due to the rewiring of one of the crossings in the trefoil knot. The second decay process *Solomon link* $\Rightarrow$ *double Hopf necklace* is due to the splitting of one of the two loops interlaced twice into two loops.

(10) In the last section 11 we show first that the genesis and decay schemes unveiled in our experiments are different from those in other systems. Finally, we mention that the multiple Hopf necklaces can be obtained by strong mechanical perturbation of the system of the concentric loops.

2. Emission of disclination loops in twisted nematic layers

2.1. Friedel-de Gennes conjecture

In a short note published in 1969 [10] Jacques Friedel and Pierre-Gilles de Gennes conjectured that emission of a disclination loop of rank $m = 1/2$ should occur in a nematic layer submitted to a large enough twist distortion. They considered a layer of thickness h, confined between two parallel surfaces providing a strong planar anchoring conditions for the director $\vec{n}$, such as the one represented in Figure 2a but without the $\pm 1/2$ defects that we will take into account in the next section.

Initially the two anchoring directions are parallel to the y axis so that the angle ϕ between them and the y axis is zero. In equilibrium, the director field $\overrightarrow{n}(z) = [\cos\phi(z), \sin\phi(z), 0]$ compatible with these boundary conditions is uniform $\phi(z) = 0$.

When the upper surface is rotated by an angle $\delta\phi$ in anticlockwise direction, the director field in equilibrium can adopt two helical configurations compatible with the anchoring conditions (see Figure 2d):

$$\phi(z)_d = \delta\phi\frac{z}{h}; \quad \text{dextrogyre twist} \tag{1}$$

and

$$\phi(z)_l = (\delta\phi - \pi)\frac{z}{h}; \quad \text{levogyre twist} \tag{2}$$

The elastic energy density per unit area of these excited helical states depends on $\delta\phi$.

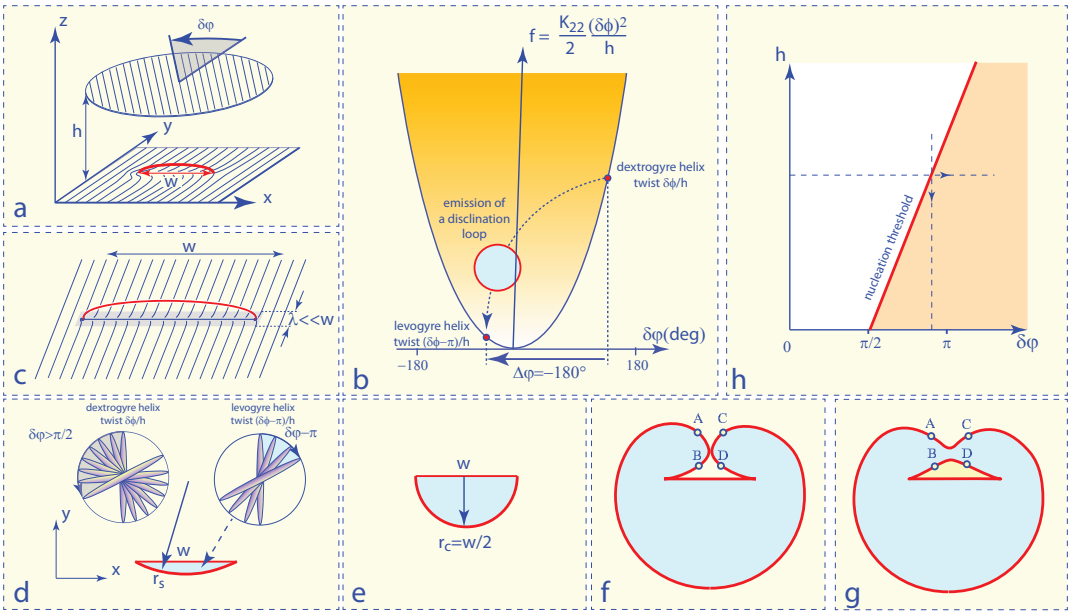

Figure 2. Experimental confirmation by Long et al. [11] of the Friedel - de Gennes conjecture [10] about the emission of disclination loops in a twisted enough nematic layer. a) Perspective view of the experiment of Long et al. [11]. b) Variation of the elastic energy density per unit surface with the angle $\delta\phi$ of rotation of the upper surface with respect to the lower one. c) Simplified anchoring pattern containing the $\pm 1/2$ singularities. d) Top view of a small deformation of the disclination segment due to the rotation of the upper surface by the angle $\delta\phi > \pi/2$. e) Semi-circular shape of the dislocation with radius $r_c = w/2$ at the threshold of the emission. f) Self-collision of the strongly deformed disclination loop. g) Rewiring of the colliding disclination segments results in emission of an independent disclination loop. h) Stability diagram. The threshold line can be crossed either by increasing the angle $\delta\phi$ or by decreasing the thickness h.

The energy of the dextrogyre helix

$$f_d = \frac{K_{22}}{2}\frac{\delta\phi^2}{h} \tag{3}$$

grows with $\delta\phi$ (see Figure 2b) while that of the levogyre helix

$$f_l = \frac{K_{22}}{2}\frac{(\pi - \delta\phi)^2}{h} \tag{4}$$

decreases initially with $\delta\phi$.

For $\delta\phi > \pi/2$, the energy density f_l of the levogyre helix becomes lower than that of the dextrogyre one, f_d.

For this reason, Jacques Friedel and Pierre-Gilles de Gennes conjectured in their paper that the elastic energy stored in the dextrogyre helix could relax through emission of a disclination loop of rank $m = 1/2$ surrounding the domain with the levogyre helix.

They also remarked that the emission of the disclination loop is protected by a nucleation barrier resulting from the competition between the gain in the surface energy and the cost of the disclination line. For a loop of radius r, the change of the

distortion energy inside it

$$\Delta E_{surf} = \pi r^2 (f_l - f_d) = \pi r^2 \frac{K_{22}\pi}{h}(\pi/2 - \delta\phi) \tag{5}$$

is negative for $\delta\phi > \pi/2$ while the energy cost of the disclination line of tension T (energy per unit length) is

$$\Delta E_{line} = 2\pi r T \tag{6}$$

The total change of energy $\Delta E_{loop} = \Delta E_{surf} + \Delta E_{line}$ has a maximum at

$$r_{max} = h\frac{T}{K_{22}\pi}\frac{1}{\delta\phi - \pi/2} \tag{7}$$

of height

$$\Delta E_{max} = \frac{hT^2}{K_{22}}\frac{1}{\delta\phi - \pi/2} \tag{8}$$

At the end of their article, Friedel and de Gennes suggested that surface defects could help to overcome this energy barrier that hinders the nucleation of the disclination loop.

2.2. Frank-Reed mechanism of nucleation of disclination loops, experiment of Long et al.

The Friedel-de Gennes conjecture was verified in a recent experiment performed by Long at al.[11] who used as the nucleation center a pair of $\pm 1/2$ surface defects, separated by the distance w, obtained by an adequate patterning of the planar anchoring on the lower limit surface (see Figure 2a). The planar anchoring on the upper surface is uniform. This upper surface can rotate around the vertical axis z by the angle $\delta\phi$. At the beginning of the experiment, at $\delta\phi = 0$, a segment of a $m = 1/2$ disclination is stretched, for topological reasons, between the surface defects.

Long at al. observed that upon a continuous increase of the twist angle $\delta\phi$, the disclination observed from above bows and expands in the plane (x,y) as shown in Figures 2d-f until the collision of its AB and CD segments defined in Figure 2f occurs. This self-collision of the disclination loop leads to the rewiring process $AB + CD \Rightarrow AC + BD$ depicted in Figure 2f and, finally, results in generation of an independent disclination loop.

The paper by Long at al.[11] contains a very detailed theoretical discussion of this experiment which is quite subtle when one takes into account the 2D anchoring pattern in the vicinity of the $\pm 1/2$ singularities. For the sake of simplicity, we will suppose that the two point defects $\pm 1/2$ are connected by a narrow surface wall of the width λ much smaller than the distance w between the defects. Upon crossing this surface wall, the anchoring direction rotates by π.

Let us consider now the small bowing deformation of the disclination segment shown in Figure 2d. It leads to creation of the lens-shaped domain of the surface area S with the levogyre twist distortion $(\delta\phi - \pi/2)/h$ surrounded by the field with the dextrogyre

twist distortion $(\delta\phi)/h$. It is obvious from equations 3 and 4 that for $\delta\phi < \pi/2$ one has $f_l > f_d$ so that such a domain cannot be stable.

For $\delta\phi > \pi/2$, the expansion of the levogyre domain is favored by the inequality $f_l < f_d$ but at the same time it is limited by the energy cost of the elongation of the bow-shaped disclination. The equilibrium shape can be found from the balance of the Peach-Koehler force par unit length orthogonal to the disclination (this force acting on dislocations in stressed crystals or liquid crystals is discussed in all details by Long and Selinger in ref. [14]):

$$f_{PK} = f_d - f_l = \frac{\pi K_{22}}{h}(\delta\phi - \pi/2) \tag{9}$$

with the Laplace force

$$f_{Laplace} = -\frac{T}{r} \tag{10}$$

Using $f_{PK} + f_{Laplace} = 0$ one obtains:

$$\frac{h}{r} = \frac{K_{22}}{T}\pi(\delta\phi - \pi/2) \tag{11}$$

This relation agrees with the equation 6 from ref.[11] in the approximation $\phi_B = \pi/2$. It tells that the radius of curvature r of the lens-shaped disclination decreases with the growing twist angle $\delta\phi$. As long as r is larger then $w/2$, the lens-like shape of disclination is stable. For $r = w/2$, the disclination takes the semicircular shape shown in Figure 2e. Upon a further increase of the twist angle $\delta\phi$, the disclination loop expands so that its radius increases. To satisfy now the equilibrium condition given by equation 11 the twist angle $\delta\phi$ should be reduced. Even if this can be done experimentally, this new equilibrium is unstable.

The stability limit of the lens-shaped disclination is thus given by $r_c = w/2$. By substitution of this relation in equation 11, one obtains:

$$h_c = C(\delta\phi - \pi/2) \tag{12}$$

with

$$C = \frac{w}{2}\frac{K_{22}}{T}\pi \tag{13}$$

The stability limit given by equation 12 is plotted in Fig.2h.

In the experiment of Long et al. this limit was crossed by increasing the twist angle $\delta\phi$ at $h = const.$ **Remark 1**: The slope C decreases with the distance w between the anchoring singularities. Therefore, the critical angle $\delta\phi$ at which the nucleation occurs can be much larger than π when w is small. In such a case the twist distortion $(\delta\phi - \pi)/h$ inside the dislocation loop is dextrogyre like outside of the loop but its amplitude is smaller.

Alternatively, the stability limit can also be crossed by decreasing the thickness h (i.e. by compression of the twisted cell) at $\delta\phi = const.$ This second method of nucleation of disclination loops by compression of the twisted cell is analogous to the nucleation of dislocation loops reported previously [8,15] and in sections 6 and 7 below.

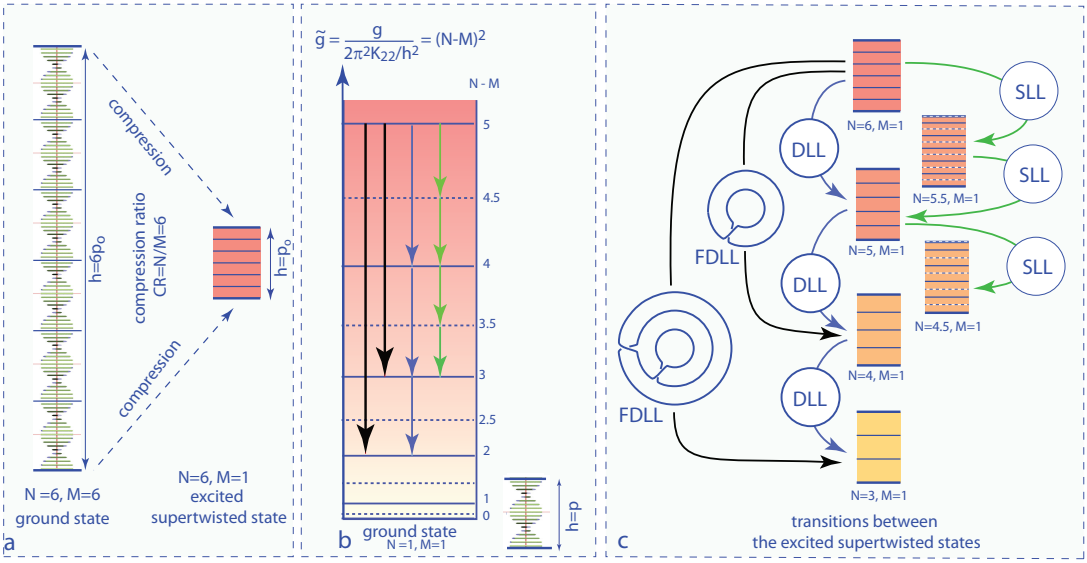

Figure 3. Reformulation of the Friedel-de Gennes conjecture to the case of emission of dislocation loops in supertwisted cholesteric layers. a) Production of an excited supertwisted state by a sixfold compression of the ground state containing six full turns of the cholesteric helix. b) Discrete energy levels have two indices: N- the number of 2π turns of the helix between the limit surfaces and $M = h/p$- the number of cholesteric pitches that can be accommodated without distortion inside the layer. c) Transitions with $\Delta N = 1/2$ result in emission of dislocation loops called SLL with the Burgers vector $b = p/2$, while those with $\Delta N = 1$ should generate dislocation loops called DLL with the Burgers vector $b = p$ (see Figures 4e and 4f). The black arrows correspond to a serial nucleation of two and three DLL loops connected by crossings into the folded double line loops (FDLL). (see Figures 1 and 21) .

Remark 2: At first sight, the nucleation of disclination loops by the compression of the twisted cell (with $\delta\phi$ kept constant) seems to be similar to the nucleation of dislocations in a crystal slab submitted to a compressive strain. However, there is a huge quantitative difference between these processes. The elastic limit of crystals in terms of the strain is small: if the initial thickness of the crystal slab is h_o then the nucleation occurs when the change of the thickness Δh is of the order of a few percent of h_o. In nematics, the elastic limit is given by equation 12. The critical thickness h_c depends on the twist angle $\delta\phi$ but not on the initial thickness h_o of the nematic layer. Therefore, the compression ratio h_o/h_c can be infinite when $h_o \Rightarrow \infty$.

3. Principle of the emission of dislocation loops in supertwisted cholesteric layers

3.1. Supertwisted cholesterics

In experiments reported here, instead of the twisted nematic, we used a cholesteric layer of thickness h confined between mica surfaces providing a planar anchoring (see Figure 3a). We consider this anchoring as strong because in conditions of our experiments (samples with large cholesteric pitches p_o) the elastic torques exerted on surfaces are not large enough to alter much the direction of the anchoring or to trigger the breaking of the anchoring reported by Angelo et al. [16].

The elastic energy density per unit volume of this system can be expressed as :

$$g_N = \frac{K_{22}}{2}\left(\frac{N2\pi}{h} - \frac{2\pi}{p_o}\right)^2 = \frac{2\pi^2 K_{22}}{h^2}(N-M)^2 = \frac{2\pi^2 K_{22}}{p_o^2}\left(\frac{N}{M} - 1\right)^2 \qquad (14)$$

where N is the number of full cholesteric pitches lodged between the mica surfaces, p_o is the natural pitch of the cholesteric helix and $M = h/p_o$ is the layer thickness expressed in units of p_o.

The cholesteric helix is said to be **supertwisted** when N is larger then M. The difference N-M measures the degree of the supertwist and the energy density per unit volume, given by equation 14, varies as $(N-M)^2$.

Alternatively, N/M could be used as the measure of the supertwist because it is equal to the ratio p_o/p between the natural pitch p_o and the pitch $p = h/N$ imposed by the confinement. In this article, to quantify the supertwist, we will use this second method with **the compression ratio CR** defined as $CR = N/M = p_o/p$. In the example shown in Figure 3a where $N/M = 6$, the natural cholesteric pitch p_o is compressed to $p = p_o/6$.

Experiments reported in section 7 start from the ground state of cholesteric layers in which $M = N$ (like the one in Figure 3a). The supertwisted excited states are then reached by compression of the layer thickness from $h = Np_o$ to a smaller value $h = Mp_o$ with M smaller than N.

3.2. Reformulation of the Friedel-de Gennes conjecture

In the case of such supertwisted cholesteric layers, the Friedel-de Gennes conjecture can be reformulated as follows: **transitions between the discrete energy levels of a supertwisted cholesteric layer should be mediated by emission of dislocation loops** (see Figure 4c).

In terms of the classification elaborated by Kleman and Friedel [12,15], two types of dislocations can be emitted during transitions between the supertwisted states (see Figures 4d, 4e and 4f). Those with the Burgers vector $b = p/2$ are called **single** (SL), have optical aspect of **thin** lines and are equivalent to $m = 1/2$ disclinations [12,15,17]. Dislocations with the Burgers vector $b = p$ are called **double** (DL), they appear in microscope as **thick** lines and are equivalent to disclinations of rank $m = 1$ [12,15,17]. We will use this terminology, SL and DL, in the rest of this paper.

3.3. Former studies of nucleation of dislocation loops

Nucleation of dislocation loops in supertwisted cholesteric layers was reported previously by Zappone and Bartolino [13], by the authors in ref. [8] as well as by one the authors in ref. [15].

Zaponne and Bartolino, who used a surface force apparatus, reported on the emission, induced by a compressive strain, of the simple dislocation loops with the Burgers vector $b = p/2$.

Our observations reported in ref. [15], made with a different setup, tailored for observation of dislocations in cholesterics (see section 4), showed that beside dislocation loops with the Burgers vector $b = p/2$, dislocations with the Burgers vector $b = p$ could also be nucleated upon a compressive strain. Moreover we have found that several different modes of nucleation of dislocation loops were possible:

Individual mode: In the *individual mode*, dislocation loops were nucleated one after another. From topological point of view, such individual loops are equivalent to trivial unknots.

Serial mode: In the *serial mode* several dislocation loops, nucleated in one burst, were connected by crossings into one superloop which from topological point of view is equivalent to a multiply folded (twisted) unknot. Zappone and Bartolino [13] reported that such serial nucleation of dislocation loops occurred also in their surface force apparatus.

Continuous mode: In the continuous mode, one superloop is generated by the mechanism similar to the Frank-Reed mechanism with this difference that the extremities of the dislocation loop, attached to the surface of a large dust particle, are located at different levels. In this geometry, the self-collision of the dislocation resulting in the coalescence-rewiring process (see Figures 2f and 2g) does not occur.

4. Setup and methods

Our setup is depicted schematically in Figure 4a-c. It was tailored specifically for optical observations of dislocations in cholesterics and proved more recently to be very convenient for experiments on the nucleation of dislocation loops. It has the same crossed cylinders geometry as that of the surface force apparatus used by Zappone and Bartolino[13].

Freshly cleaved rectangular ($25 \times 37mm$) thin ($0.1mm$) mica sheets are fixed mechanically on plastic curved supports (see Figure 4b). One support, equipped with a mica sheet, is located on a plate which is mobile in x and y direction (see Figure 4c). The second support, equipped with a mica sheet, is attached to a rotating table positioned on a second plate which is mobile in z direction by means of a precision translation stage. The screw of the stage is rotated by means of a long lever coupled by a yarn to a cylinder rotated by a stepping motor. The precision of this vertical motion is 0.15 or $0.3\mu m$ per step.

Experiments were performed with mica sheets free of inclusions and cleaved carefully with the aim to avoid as much as possible dust particles and surface steps. For the same reason, cholesteric mixtures were prepared from filtered 5CB and CB15 materials. Their pitches $p_o = 3.48\mu m$ and $p_o = 10\mu m$ are much larger than the pitch $p_o = 0.244\mu m$ of the cholesteric (YPDLC-036/R2011) used by Zappone and Bartolino[13].

The lines of the equal thickness $h(x, y) = const$ of the gap between cylinders are in general elliptic and depend on the radii of curvature R of the cylindrical mica sheets as well as on the angle between the axes x and x' of cylinders. In experiments presented below, the radii of curvature of the two mica sheets were the same (R=50mm) so that the lines of equal thickness should be circular if the cylinders were orthogonal as shown in Figure 4a. The elliptic shapes of dislocation lines, for example in the experiment 1 in Figure 8, are due to a deviation from the perfectly orthogonal configuration.

5. Types and indexing of dislocations in cholesterics

Two typical nets of dislocation loops generated with our crossed cylinders setup are shown in Figure 5a and 5b. Indexing of dislocation lines in these pictures is a quite subtle issue for several reasons:

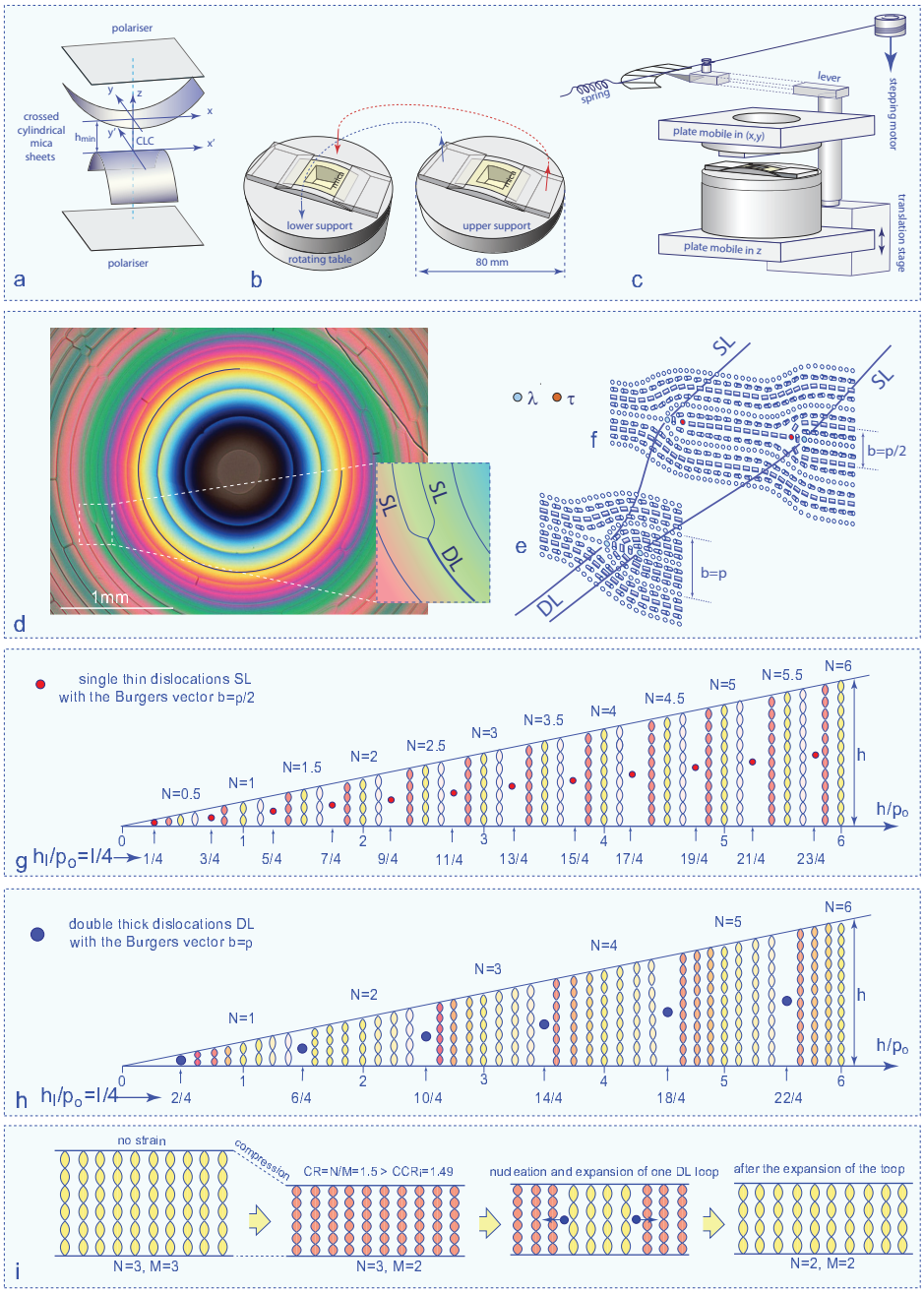

Figure 4. Systems of dislocations in confined cholesteric layers. a) Crossed cylinders geometry. The anchoring directions on the lower and upper mica sheets are the same: x//x'. b) Supports of mica sheets. c) Perspective view of the setup. d) Pattern of dislocations in the crossed cylinders geometry. e-f) Director field of the double and single dislocation lines proposed by M. Kleman and J. Friedel in their seminal article [12]. g-h) Indexing convention of single and double dislocation lines. For the sake of simplicity the case of a plane/plane wedge is depicted here. N indicates the number of full 2π turns of the cholesteric helix lodged between the limit surfaces. I is the index of dislocations in the wedge. M=h/p is the local reduced thickness of the gap. It can be also seen as the number of cholesteric pitches that could be lodged between limit surfaces without distortion. i) Process of emission of one double line loop. Compression of the (N=3,M=3) ground state leads first to the excited (N=3,M=2) state. When the compression ratio CR=N/M=3/2 exceeds the critical value CCR_i, emission of one double line loops occurs and the new ground state (N=2,M=2) is reached.

(1) At first sight, systems of dislocation lines appear as composed of concentric circles but this does not mean that each circle corresponds to one dislocation loop. As we will see below, such a scheme is quite rare and occurs only when dislocations are nucleated one after the other.
(2) For topological reasons, dislocation lines must be closed (if they do not end on surfaces) but this does not mean that each dislocation line has the shape of one circle. In fact one dislocation line starting from a point P can pass several times from one circle to an adjacent circle but finally it must return to the point P. For this reason, dislocation lines self-intersect frequently. Such self-intersections are present in the loops folded once in Figure 1a or twice in Figure 1b. Due to the helicoidal symmetry of cholesterics, intersections of dislocations are almost always stable [15].
(3) When the minimal distance h_{min} between cylinders vary, the radii of circles change. They decrease when h_{min} grows so that circles collapse one after another. Inversely, when h_{min} decreases, the radii of circles increase and new dislocations can be nucleated in the gap.
(4) Collapse of dislocation is free but nucleation of new loops is protected by the nucleation barrier. For this reason, the elasticity of cholesteric layers is highly asymmetric [13].
(5) In the absence of bifurcations (splitting of one double line into two single lines, see Figure 4), single and double dislocation lines can coexist indefinitely independently of the thickness of the gap because the splitting $DL \Rightarrow SL + SL$ and merging $SL + SL \Rightarrow DL$ processes are protected by energy barriers.

In this situation, the method of indexing of the disclination loops that appeared to us as the most convenient and unambiguous uses the general expression for equilibrium thicknesses accessible for single and double dislocations (see ref.[15]):

$$h_I(r) = \frac{p_o}{4}\left[I - \frac{\delta\psi}{\pi/2}\right] \tag{15}$$

with I=1,3,5,... for single dislocation lines and I=0,4,8,... or 2,6,10,... for double dislocation lines. $\delta\psi$ is the angle between the anchoring directions on the lower and upper mica sheets. Let us note that in fields between dislocation lines the twist angle of the cholesteric helix must be:

$$\Delta\psi_N = 2\pi N + \delta\psi \tag{16}$$

with N=0,1/2,1,3/2,...

To be more explicit, let us consider nets of dislocations shown in Figures 5a and b. Here, the thickness of the gap is zero in the centre and it grows as $h(r) = r^2/(2R)$ with the radius r. The indexing of lines crossing the dashed lines in Figures 5a and b was made as follows:

- The line closest to the centre is of the single (thin) type, therefore its index is I=1.
- The second line in the picture a is also single so that its index is 3.
- The third line is double. Is its index 4 or 6? It cannot be 4 because the twist angle in the field after the second line must be $\Delta\psi_4 = 2\pi$. In conclusion, it can only be 6.

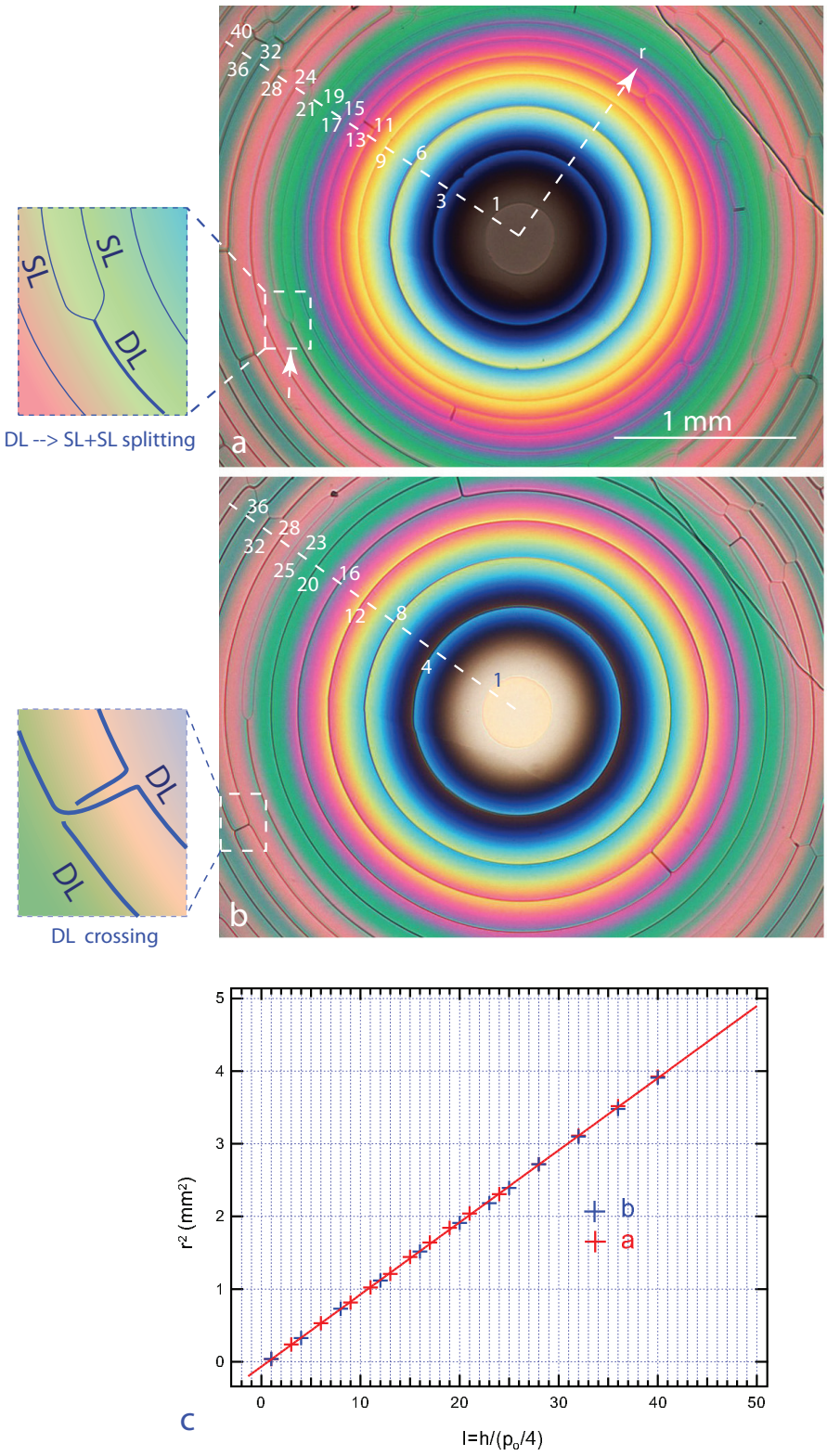

Figure 5. Patterns of single and double dislocation loops in the cylinder/cylinder geometry. a-b) Indexing and measurement of the radii of disclinations. c) Fit to the linear law given in equation 17.

In general, the indexing of lines can be made easily using the following rules:

(1) upon passing from a single to another single line, the index I increases by 2,
(2) upon passing from a single to a double line, the index I increases by 3,
(3) upon passing from a double to a single line, the index I increases by 3,
(4) upon passing from a double to another double line, the index I increases by 4.

After determination of the indices I, the radii r_I of dislocation loops have been measured on pictures a and b in Figure 5. Values of r_I^2 are plotted versus the index I in Figure 5c.

In approximation of small enough tension of dislocations (see section 8.1), the local thickness h_I at positions r_I of disclinations should satisfy the geometrical relationship

$$h_I = \frac{r_I^2}{2R} \tag{17}$$

as well as the equation 15. In result, the following linear relationship should be satisfied:

$$r_I^2 = \frac{Rp_o}{4}\left(I - \frac{\delta\psi}{\pi/2}\right) \tag{18}$$

The continuous line in Figure 5c represents the linear fit to this equation with $R = 50$ mm, $p_o = 3.48\mu m$ and $\delta\psi = 60°$.

6. Emission of individual single disclination loops

Emission of independent single dislocation loops, one after another, during slow reduction of the minimal distance between the crossed cylindrical mica sheets appeared in our experiments as quite rare while nucleation of double dislocation loops was much more frequent. Nevertheless, as it corresponds to the Friedel - de Gennes conjecture and was observed by Zappone and Bartolino [13], it deserves a detailed discussion based on one typical experiment.

The picture in Figure 6a shows a view of the central part of the cylinder/cylinder gap containing single line loops indexed with integers I ranging from 1 to 21, following the convention depicted in Figure 4g. This pattern, made of separated (i.e. without crossings) single line loops, is the result of emission of individual loops during a slow reduction of the gap thickness at the rate of $0.015\mu m/s$ (see the plot in Figure 6b). We measured the radii r_I of the 21 loops in this image and from the plot r_I^2 vs I we have found that in this experiment the angle $\delta\psi$ between the anchorings was close to $\pi/2$.

The emission and annihilation processes occurring during the slow variation of the cylinder/cylinder gap were recorder as a time laps movie at the rate of 1 image per second. Using the ImageJ software, the diagonal line CS defined in Figure 6a was extracted from each frame of the video. The resulting 3000 lines were stacked in horizontal direction. The spatio-temporal cross section extracted from the time laps movie is shown in Figure 6c.

The left half of this picture (reduction of the gap thickness) shows that dislocation loops were nucleated one after another on the dust particle visible in the series of four pictures (d).

The right half of the Figure 6c shows that upon the regular increase of the

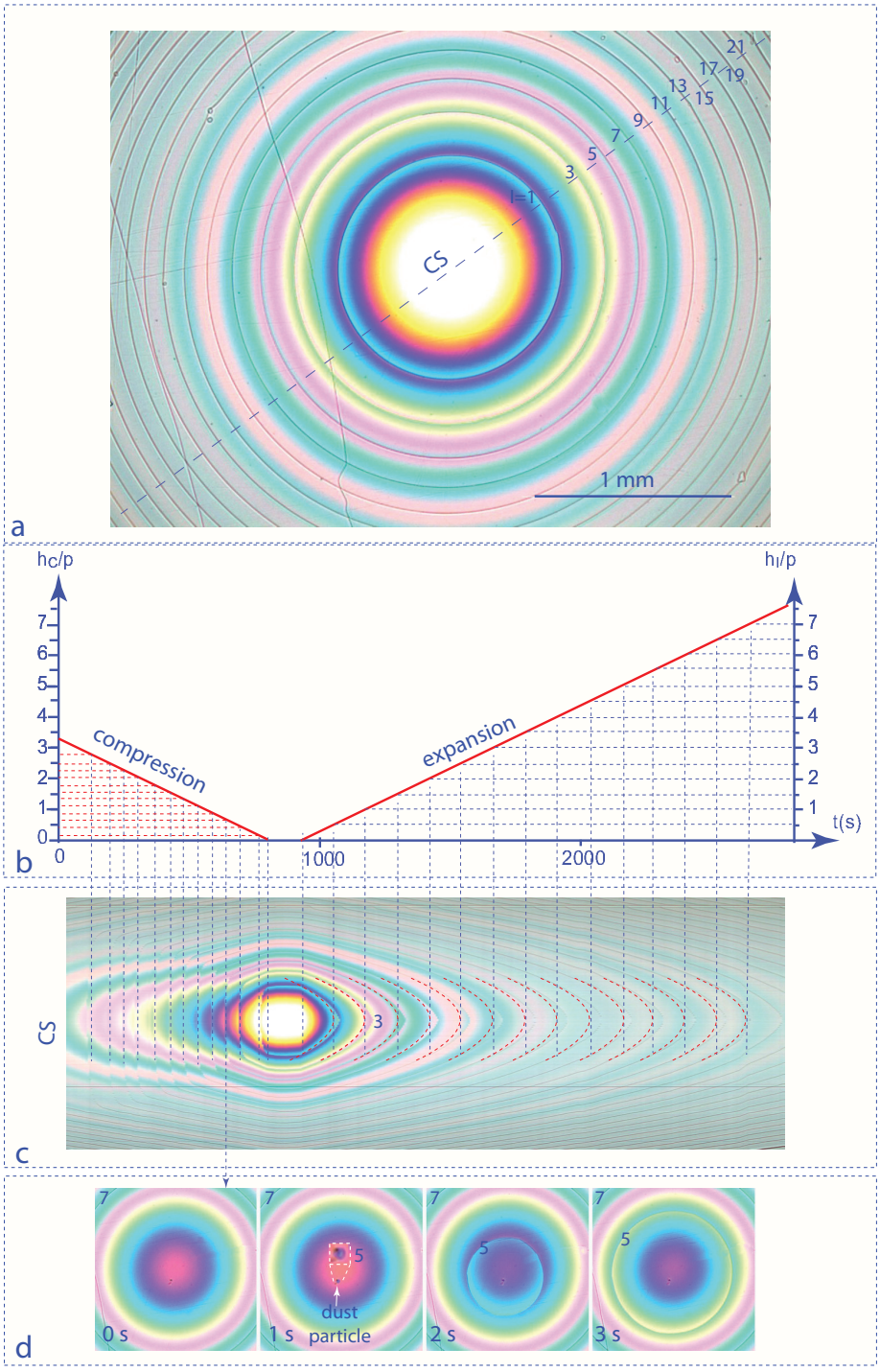

Figure 6. Nucleation of individual single dislocations loops, one after the other, on a dust particle. a) Dislocation loops labeled with the index I=1,3,...,23 (defined in Figure 4g) are independent. They were nucleated on the dust particle indicated in the picture (d) by the arrow. b) Linear variation of the minimal gap thickness h_{min} in time. The rate of variation is $\mp 0.015 \mu m/s$. c) Spatio-temporal cross section extracted from a video along the line CS defined in (a). d) Pictures of the dislocation loop with the index I=5 taken at intervals of 1 s during expansion after nucleation on the dust particle. The pitch of the cholesteric helix in this experiment is $p_o = 10 \mu m$.)

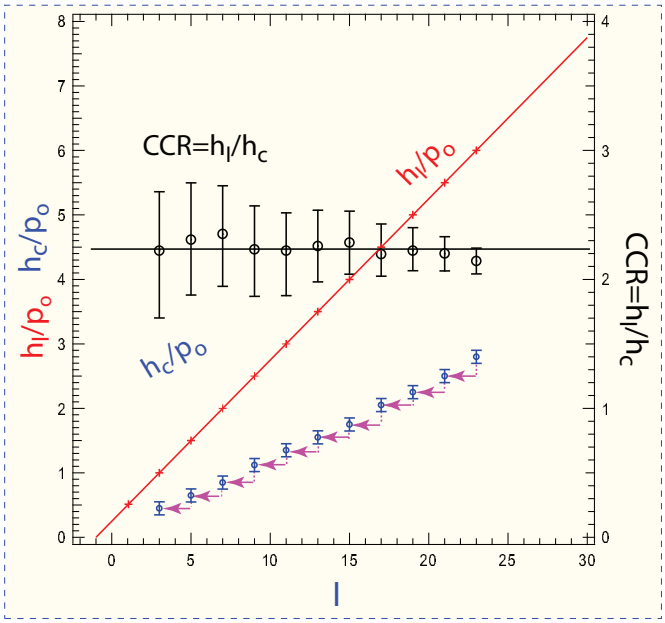

Figure 7. Determination of the critical compression ratio $CCR = h_I/h_c$ for the emission of individual single dislocation loops in the experiment depicted in Figure 6. In this experiment the anchorings make the angle $\delta\psi \approx \pi/2$. The thickness h_I is given by the equation 15 : $h_I = I(po/4) + 1/4$. h_c is the thickness at which the dislocation loop with the index I is nucleated.

gap thickness, the dislocation loops shrink and finally collapse smoothly. The rate $dh_{min}/dt = 0.015\mu m/s$ is so small that the size of loops during their shrinking is close to equilibrium. However, a closer look at the spatio-temporal cross section unveils that trajectories of the collapsing dislocation loops do not coincide with trajectories of isochromes i.e. of lines of constant gap thickness.

To be more precise, let us compare the trajectory of the dislocation with the index I=3 with the trajectory of the isochrome in its vicinity indicted with a dashed thick red line. Clearly, the trajectory of the dislocation is retarded with respect to that of the isochrome and the retardation grows when the dislocation approaches the center of the cylinder/cylinder gap where the variation of the Peach-Koehler force (given in equation 22) with the radius r tends to zero.

For this reason, in Figure 6c, ideal, non retarded trajectories of dislocations are indicated with dashed thin lines. In terms of the model presented in section 8.1, the reduced gap thickness at which the I-th dislocation is in equilibrium (the Peach-Koehler force vanishes) is given by $h_I = (p_o/4)(I - \delta\psi)/(\pi/2)$..

Using this property, the gap calibration is done graphically using Figures 6b and c. The corresponding values of h_I/p_o are plotted versus I in Figure 7 (red crosses). The red line with the slope 1/4 corresponds to the equality $h_I = (p_o/4)(I + 1)$.

The left half of the spatio-temporal cross section in Figure 6b is not symmetric with respect to the right half because there is a barrier for nucleation of dislocation loops occurring during the compression of the gap. The values of the reduced thickness h_c/p_o at which nucleation of dislocation loops occurs are plotted with blue crosses in Figure 7. The staircase-like line in this graph visualises the sequence of events in this experiment. The vertical dashed lines correspond to the slow compression of the cylinder/cylinder gap. The horizontal arrows represent emissions of single dislocation

loops leading to the reduction of the index I by 2.

The critical compression ratio $CCR = h_I/h_c$ is plotted in Figure 7 with black circles. Remarkably, it is almost constant with the mean value $< CCR >= 2.2$.

For the purpose of the forthcoming discussion in section 9.1. "Nucleation of SL loops on the pair of $\pm 1/2$ anchoring defects" let us note that the nucleation centre is well visible in the picture labeled 1s in Figure 6d. Its radius is of the order of $p_o = 15\mu m$.

7. Emission of individual double disclination loops

As the emission of individual double lines loops is more frequent then that of single lines loops, we were able to perform several experiments of this kind. For the purpose of this article we selected three experiments differing by the size of the nucleation centre. Their results are presented in Figures 8, 9 and 10 using the scheme similar to that of Figure 6.

7.1. Experiment 1

The picture in Figure 8a shows a view of the central part of the sample containing double line loops indexed with integers I ranging from 10 to 42, following the convention depicted in Figure 4h. **Remark:** In this picture, the thickness in the centre of the cylinder/cylinder gap is not zero.

The spatio-temporal cross section extracted along the line CS defined in (a) from a video recorded in this experiment is shown in Figure 8c.

The left half of this picture (reduction of the gap thickness) shows that dislocation loops were nucleated one after another on the dust particle indicated by an arrow in the picture (a) and which appears as the horizontal black line in the spatio-temporal cross section. Let us note that this nucleation centre is shifted with respect to the centre of the cylinder/cylinder gap.

The right half of the Figure 8c shows that upon the regular increase of the gap thickness, the dislocation loops shrink and finally collapse smoothly. For calibration of the reduced gap thickness h_I/p_o at the position of the dust particle we used intersections of dislocations' trajectories with the horizontal trajectory of the dust particle. In terms of the equation 15, the reduced gap thickness at which the I-th dislocation is in equilibrium (the Peach-Koehler force vanishes) is given by $h_I = (p_o/4)(I - \delta\psi/(\pi/2))$.

Within the approximation $\delta\psi = 0$, the gap calibration is done graphically using Figures 8b and c. The corresponding values of h_I/p_o are plotted versus I in Figure 11a (red crosses). The red line with the slope 1/4 corresponds to the equality $h_I/p_o = I/4$.

From the left half of the spatiotemporal cross section in Figure 8b we determined the values of the reduced thickness h_c/p_o at which nucleation of dislocation loops occurs. They are plotted with blue crosses in Figure 11a. The staircase-like line in this graph visualises the sequence of events in this experiment. The vertical dashed lines correspond to the slow compression of the cylinder/cylinder gap. The horizontal arrows represent emissions of dislocation loops leading to reduction of the index I by 4.

The critical compression ratio $CCR = h_I/h_c$ is plotted in Figure 11a with black circles. Remarkably, it is almost constant with the mean value $\bar{CCR} = 1.38$.

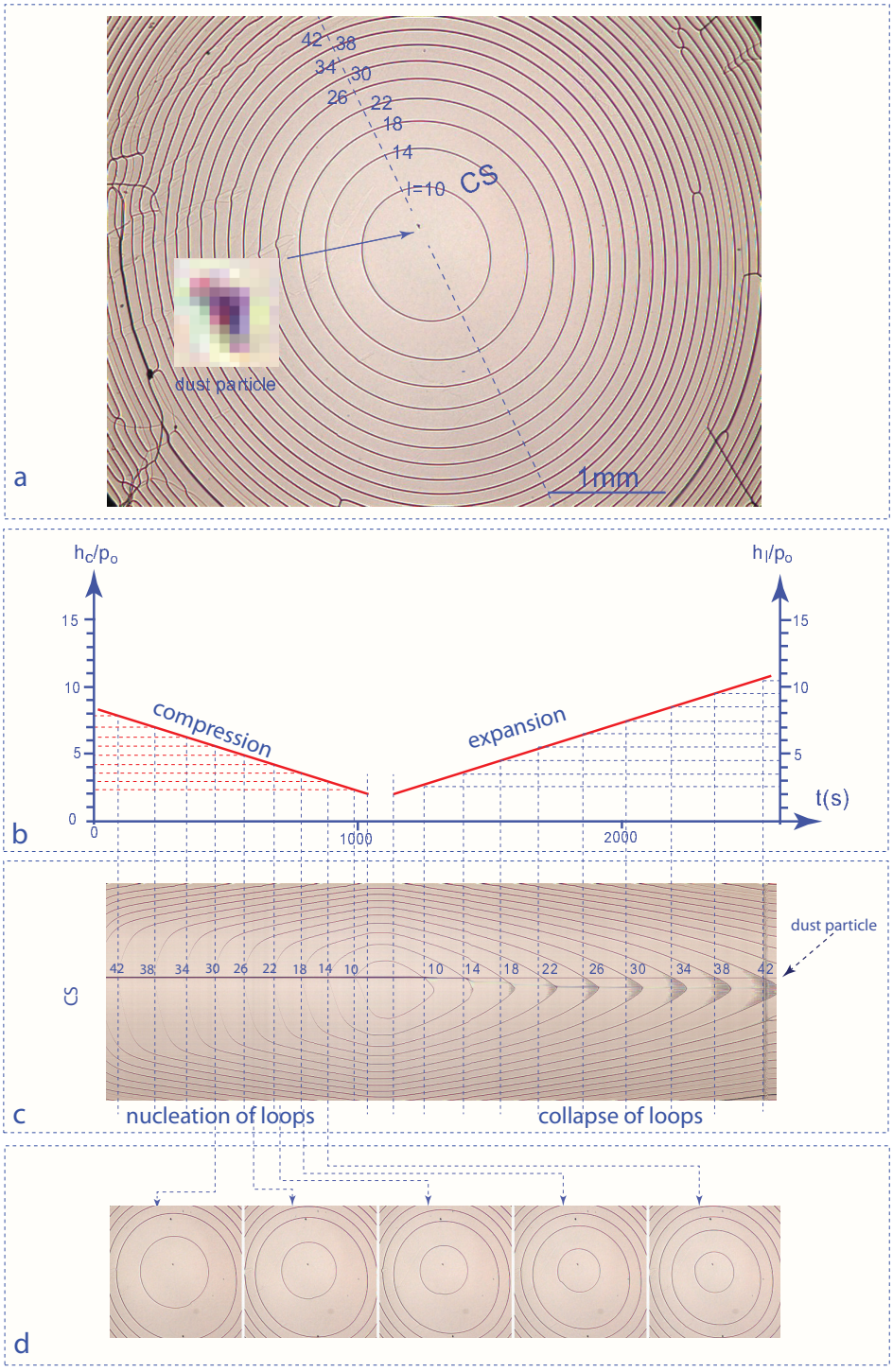

Figure 8. Nucleation of individual double dislocations loops, one after the other, on a dust particle. Experiment 1 : a) Dislocation loops labeled with the index I=10,14,...,42 (defined in Figure 4g) are independent. They were nucleated on the dust particle indicated by the arrow. b) Linear variation of the minimal gap thickness h_{min} in time. The rates of the thickness variations are $dh/dt \mp 0.03\mu m/s$. c) Spatio-temporal cross section extracted from a video along the line CS defined in (a). d) Pictures of dislocation loops taken during their expansion after nucleation on the dust particle. In this experiment, polarisers were removed. The pitch of the cholesteric helix in this experiment is $p_o = 3.48\mu m$.

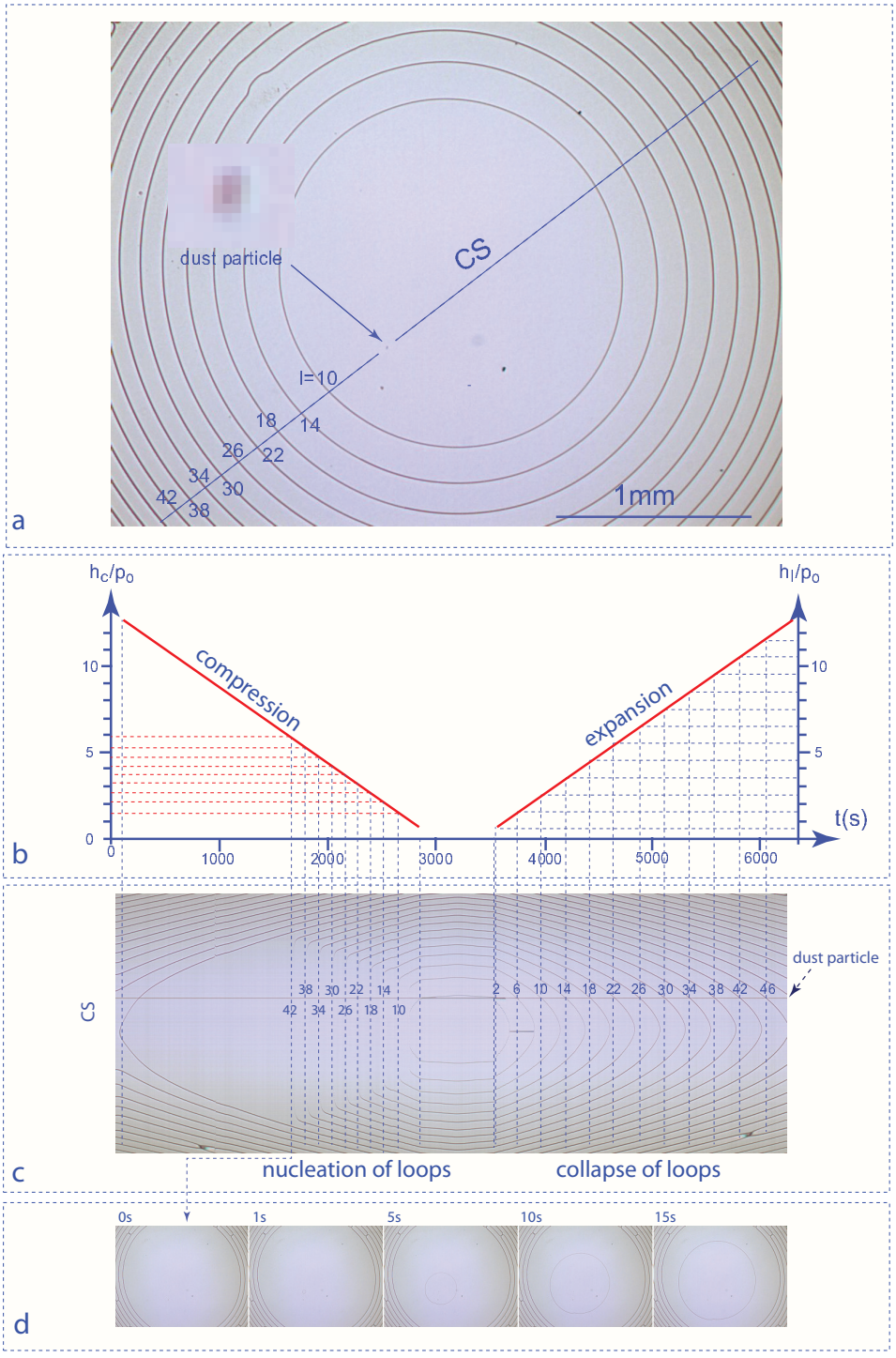

Figure 9. Nucleation of individual double dislocations loops, one after the other, on a dust particle. Experiment 2. a) Dislocation loops labeled with the index I=10,14,...,42 (defined in Figure 4g) are independent. They were nucleated on the dust particle indicated by the arrow. b) Linear variation of the minimal gap thickness h_{min} in time. The rate of the thickness variation is $\mp 0.03 \mu m/s$. c) Spatio-temporal cross section extracted from a video along the line CS defined in (a). d) Pictures of the dislocation loop N=11 taken during its expansion after nucleation on the dust particle. In this experiment, polarisers were removed and the pitch of the cholesteric helix is $p_o = 3.48 \mu m$.

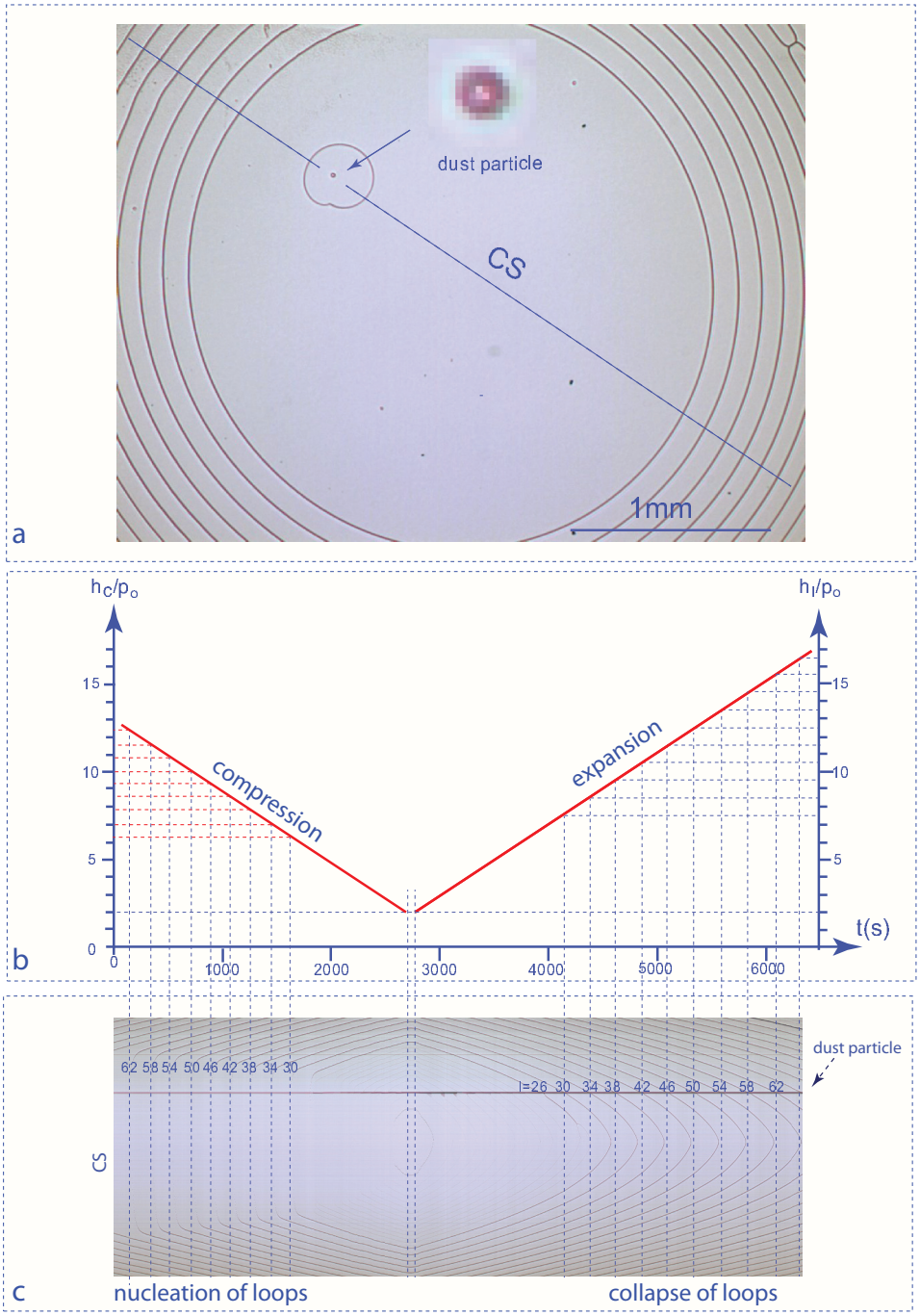

Figure 10. Nucleation of individual double dislocations loops, one after the other, on a dust particle. Experiment 3. a) Definition of the line CS used for extraction of a spatio-temporal cross section from a video. The picture shows an expanding dislocation loop nucleated on the dust particle indicated with an arrow. b) Linear variation of the minimal gap thickness h_{min} in time. It is calibrated using the right part of the spatio-temporal cross section. c) Spatio-temporal cross section extracted from a video along the line CS defined in (a). Let's note, in its central part, the presence of trajectories of single line loops (thin lines) emitted from the dust particle. They are useful for indexing of the double line loops: a pair of single lines is counted as one double line. In this experiment, polarisers were removed and the pitch of the cholesteric helix is $p_o = 3.48\mu m$.

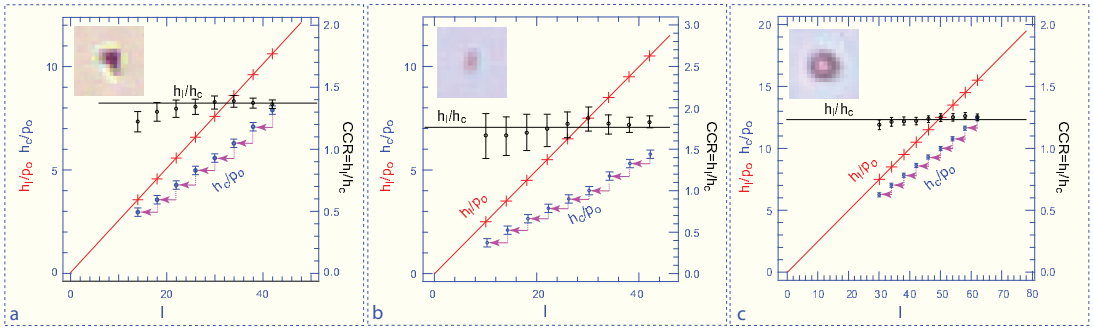

Figure 11. Determination of the critical compression ratio $CCR = h_I/h_c$ for emission of individual double dislocation loops. a) Experiment 1 in Figure 8. b) Experiment 2 in Figure 9. c) Experiment 3 in Figure 10.

7.2. Experiment 2

The second example of the emission of individual double line loops is illustrated in Figure 9. Here, the spatio-temporal cross section in the picture (c) shows that nine loops, labelled with the index I=10,14,...,46 (defined in Figure 4h), are emitted from the dust particle indicated with arrows in pictures (a) and (c). Like in experiment 1, this nucleation centre is shifted with respect to the centre of the cylinder/cylinder gap.

As above, for calibration of the gap thickness h_I/p_o in the (x,y) position of the dust particle we used the right half of spatio-temporal cross section where intersections of trajectories of collapsing loops with the trajectory of the dust particle occur for $h(I) = Ip_o/4$ (see equation 23).

After calibration, values of the critical thickness h_c/p_o at which nucleation of loops occurred were determined from the left part of the spatio-temporal cross section.

Results of this second experiment are summarized in the plot of Figure 11b.

The mean value of critical compression ratio for emission of individual loops determined from this plot $C\bar{C}R = 1.75$ is higher than $C\bar{C}R \approx 1.5$ found in the experiment 1.

7.3. Experiment 3

The third example of the emission of individual double line loops is illustrated in Figure 9. Here, the spatio-temporal cross section in the picture (c) shows that nine loops, labelled with the index N=34,38,...,66 (defined in Figure 4h), are emitted from the dust particle indicated with arrows in pictures (a) and (c). Like in experiments 1 and 2, this nucleation centre is shifted with respect to the centre of the cylinder/cylinder gap.

As previously, for calibration of the gap thickness h_N/p_o in the (x,y) position of the dust particle we used the right half of spatio-temporal cross section where intersections of trajectories of collapsing loops with the trajectory of the dust particle occur for $h(I) = I(p_o/4)$.

After calibration, values of the critical thickness h_c/p_o at which nucleation of loops occurred were determined from the left part of the spatio-temporal cross section.

Results of this third experiment are summarized in the plot of Figure 11c.

The mean value of critical compression ratio for emission of individual loops determined from this plot $< CCR >= 1.25$ is smaller than those in experiments 1 and

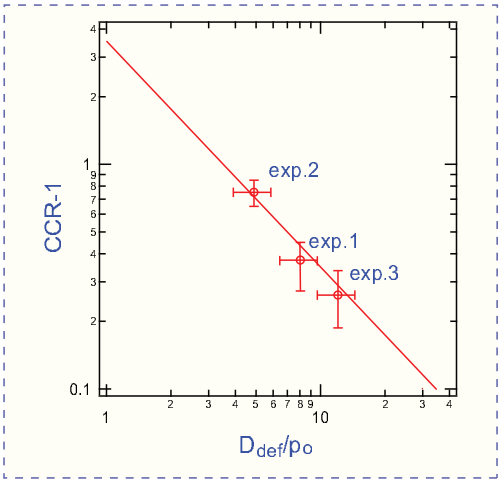

Figure 12. Plot of the critical compression ratios determined in Figure 11 versus the reduced size of defects $\tilde{D}_{def} = D_{def}/p_o$. The continuous line represents the power law $CCR - 1 = 3.5/\tilde{D}_{def}$.

2.

7.4. Critical Compression Ratio CCR

The values of the critical compression ratio CCR for nucleation of double dislocation loops determined in Figures 11a, 11b and 11c are respectively: 1.38 (exp.1), 1.75 (exp.2) and 1.25 (exp.3). At first sight, they depend on sizes D_{def} of the nucleation centres shown in inserts of the three plots. We estimated D_{def} with accuracy of $3\mu m$ as: $43 \pm 3\mu m$ (exp.1), $17 \pm 3\mu m$ (exp.2) and $28 \pm 3\mu m$ (exp.3).

Anticipating on the theoretical models of the nucleation process presented below, in Figure 12 we plotted $CCR - 1$ versus the reduced size of defects $\tilde{D}_{def} = D_{def}/p_o$. The continuous line in this diagram represents the law $CCR - 1 = 3.5/\tilde{D}_{def}$.

8. Model of nucleation of individual loops

As the critical compression ratio CCR is a dimensionless quantity it can only be function of the dimensionless ratios $\tilde{d} = d/p_o$ and $\tilde{D} = D/p_o$ (D=2R, R is the curvature radius of mica sheets) as well as of the index I of dislocation loops:

$$CCR_I = CCR(\tilde{d}, \tilde{D}, I) \tag{19}$$

To find this scaling relationship, we will analyse the balance of forces acting on dislocation loops.

8.1. Scaling analysis of the equilibrium conditions

Let us consider a double dislocation with the index $I = 2(2N - 1)$ separating fields with $(N - 1)$ and N full pitches p of the cholesteric helix (see Figure 4h). If $h(r) = h_{min} + r^2/D$ is the local gap thickness at the r position of the dislocation then the

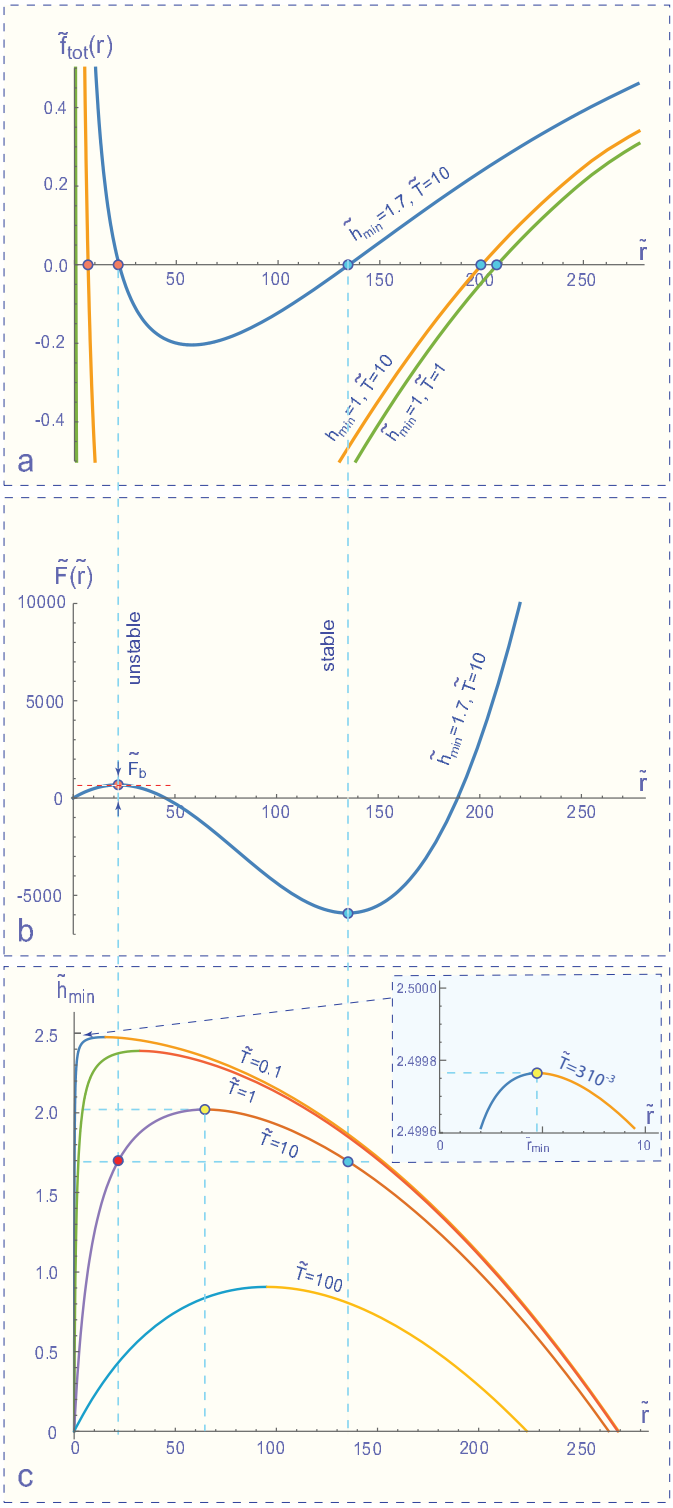

Figure 13. Scaling analysis of forces acting on the dislocation loop with I=10. a) Variation of the reduced force $\tilde{f} = f/(4\pi^2 K_{22}/p_o)$ with the reduced radius $\tilde{r} = r/p_o$ for different values of the reduced tension $\tilde{T} = T/(4\pi^2 K_{22})$ and of the reduced minimal thickness of the gap $\tilde{h}_{min} = h_{min}/p_o$. b) Variation of the reduced energy $\tilde{F}$ with the reduced radius $\tilde{r} = r/p_o$ for $\tilde{T} = 10$ and $\tilde{r}_{min} = 1.7$. c) Variation of the stable (maximal) and unstable (minimal) equilibrium radii $\tilde{r}$ of the I=10 loop with the minimal thickness of the gap $\tilde{h}_{min}$.

densities per unit surface of the elastic energy in adjacent fields are given by:

$$f_{N-1} = \frac{K_{22}}{2}\left(\frac{(N-1)2\pi}{h(r)} - \frac{2\pi}{p_o}\right)^2 h(r) \tag{20}$$

and

$$f_N = \frac{K_{22}}{2}\left(\frac{N2\pi}{h(r)} - \frac{2\pi}{p_o}\right)^2 h(r) \tag{21}$$

Their difference

$$f_{PK} = f_N - f_{N-1} = \frac{4\pi^2 K_{22}}{p_o}\left(\frac{h_I}{h(r)} - 1\right) \tag{22}$$

with

$$h_I = (4N-2)p_o/4 = Ip_o/4 \tag{23}$$

is the Peach-Koehler force per unit length acting on the dislocation with the index I. It vanishes when $h = h_I$ and is directed in outward direction when $h < h_I$ (for simplicity, we assume that the anchorings are parallel, i.e. $\delta\psi = 0$). In the case of the straight wedge shown in Figure 4g, the expression $h = h_I$ determines equilibrium positions of dislocations.

Remark: In the case of single dislocations separating fields with $N - 1/2$ and N full pitches, the factor $(N-1)$ in equation 20 should be replaced by $(N-1/2)$. With this modification, the expression 23 becomes:

$$h_I = (4N-1)p_o/4 = Ip_o/4 \tag{24}$$

In the cylinder/cylinder geometry of the gap, the dislocation has a circular shape with radius r so that it is also submitted to the centripetal Laplace force $f_{Laplace} = -T/r$ resulting from the tension T of the dislocation line.

Equation

$$f_{tot}(r) = \frac{4\pi^2 K_{22}}{p_o}\left(\frac{h_I}{h(r)} - 1\right) - T/r = 0 \tag{25}$$

representing the balance of forces depending on r can have two, one or zero solutions determined by the values of the strain $(h_I/h(r) - 1)$ and of the dislocation tension T.

Discussion of all experimental results in terms of these solution is easier when the equation 25 is rewritten, using dimensionless variables $\tilde{r} = r/p_o$, $\tilde{D} = D/p_o$, $\tilde{h}_I = h_I/p_o$ and $\tilde{h}_{min} = h_{min}/p_o$, in a dimensionless form

$$\tilde{f}_{tot} = \frac{f_{tot}}{4\pi^2 K_{22}/p_o} = \left(\frac{\tilde{h}_I}{\tilde{h}_{min} + \tilde{r}^2/\tilde{D}} - 1\right) - \frac{\tilde{T}}{\tilde{r}} = 0 \tag{26}$$

with

$$\tilde{T} = \frac{T}{4\pi^2 K_{22}} \tag{27}$$

8.1.1. General case, two solutions

As stated above, equation 26 can have two, one or zero solutions. To be more precise, let us consider the case of the dislocation with the index I=10 for which $\tilde{h}_{10} = 5/2$ and, using the values $p_o = 3.48\mu m$ of the pitch and $D = 10^5 \mu m$, let us set $\tilde{D}$ to 2.9 10^4.

In Figure 13a we show three plots of the function $\tilde{f}(\tilde{r})$. The first plot, calculated with $\tilde{T} = 10$ and $\tilde{h}_{min} = 1.7$, shows that the equation $\tilde{f}(\tilde{r}) = 0$ (see equation 26) has two solutions $\tilde{r}_1 = 134$ and $\tilde{r}_2 = 22$ indicated respectively with blue and red circles.

The first solution $\tilde{r}_1 = 134$ represents the stable equilibrium of forces acting on the loop because it corresponds to the minimum of the potential

$$\tilde{F}(\tilde{r}) = -\int_0^{\tilde{r}} \tilde{f}_{tot}(\tilde{r}) 2\pi\tilde{r} d\tilde{r} \tag{28}$$

plotted in Figure 13b.

The second solution $\tilde{r}_1 = 22$ is unstable because it corresponds to the maximum of the potential $\tilde{F}(\tilde{r})$.

The second plot of the Figure 13a was calculated with the same value of the tension $\tilde{T} = 10$ but with a smaller value of the minimal thickness : $\tilde{h}_{min} = 1$. As expected, the stable radius (blue circle) of the dislocation increases because it migrates to the thicker part of the gap. On the contrary, the unstable radius (red circle) decreases as shown.

When the tension of the dislocation and the minimal thickness tend to zero the radius of the disclination tends to its value resulting from purely geometrical considerations.

8.1.2. General case, one solution in the stability limit

For a given tension $\tilde{T} = 10$, the radius of the disclination loop depends on the minimal thickness of the gap. It is maximal, $\tilde{r} = 264$, for $\tilde{h}_{min} = 0$ (see Figure 13c). When $\tilde{h}_{min}$ increases, the loop shrinks and for $\tilde{h}_{min} = 1.7$ its radius becomes $\tilde{r} = 134$ as discussed previously (see Figure 13c).

If the tension $\tilde{T}$ was zero, the radius of the loop could shrink, being always stable, progressively to zero during the further increase of the gap thickness to its maximal value $I/4 = 2.5$ allowed for the I=10 dislocation. However, when the tension of the dislocation is finite, for example $\tilde{T} = 10$ (see Figure 13c), the stable and unstable solutions of equation 26 converge to the same value $\tilde{r} = 64$ when the minimal thickness of the gap reaches the critical value $\tilde{h}_{min} = 2.02$. For $\tilde{h}_{min} > 2.02$ the dislocation I=10 cannot be stable and must collapse.

8.2. Nucleation of dislocation loops

8.2.1. Critical radius and energy barrier

Once the I=10 loop collapsed, one can ask the question "how to restore it?". Obviously, the minimal thickness of the gap must be lowered below the critical value of 2.02. For example, the thickness can be set to the value $\tilde{h}_{min} = 1.7$ used in Figure 13c.

This condition is necessary but not sufficient for the recovery of the I=10 loop because there is the energy barrier $\tilde{F}_b$ to overcome defined in Figure 13b.

We will show now that the height of the barrier, which depends on the tension $\tilde{T}$ and on the minimal thickness $\tilde{h}_{min}$, tends to zero when $\tilde{h}_{min} \to 0$.

For the sake of simplicity we will consider the case of the infinite diameter $\tilde{D}$ for which the gap thickness does not depend on $\tilde{r}$. In this approximation, the potential $\tilde{F}$ has only one maximum corresponding to the equilibrium of forces given by the equation

$$\tilde{f}_{tot} = \frac{f_{tot}}{4\pi^2 K_{22}/p_o} = \left(\frac{\tilde{h}_I}{\tilde{h}_{min}} - 1\right) - \frac{\tilde{T}}{\tilde{r}} = 0 \tag{29}$$

which is nothing else but equation 26 in the limit $\tilde{D} \to \infty$.

The maximum of the barrier is thus situated at the dimensionless critical radius

$$\tilde{r}_b = \frac{\tilde{T}}{\left(\frac{\tilde{h}_I}{\tilde{h}_{min}} - 1\right)} \tag{30}$$

and its dimensionless height (in units of $4\pi^2 K_{22} p_o$) is given by

$$\tilde{F}_b = \frac{\pi \tilde{T}^2}{\frac{\tilde{h}_I}{\tilde{h}_{min}} - 1} \tag{31}$$

Both the critical radius and the barrier height tend to zero when the compression rate $\tilde{h}_I/\tilde{h}_{min}$ tends to infinity.

8.2.2. Can nucleation of DL dislocations be homogeneous?

In experiments reported in section 7, double line loops are nucleated at relatively small critical compression ratios $CCR_I = h_I/h_{min}$, ranging between 1.25 and 1.75, for which the height of the nucleation barrier is finite so that one can ask if nucleations of double lines could be homogeneous i.e. triggered by thermal fluctuations.

Homogenous nucleation excited by thermal fluctuations could occur if the height of the energy barrier was of the order of kT. With $K_{22} = 3{\cdot}10^{-12} N$ and $p_o = 3.48{\cdot}10^{-6} m$, the energy unit $4\pi^2 K_{22} p_o$ of the potential barrier is of the order $4 \cdot 10^{-16} J$ i.e. to $10^5 kT$ at room temperature. Using equation 31, we can say that in the best case of $CCR = h_I/h_{min} = 1.75$, the thermally excited nucleation would be possible if $\tilde{T}^2$ was of the order of $8 \cdot 10^{-6}$ or if $\tilde{T}$ was of the order of $3 \cdot 10^{-3}$.

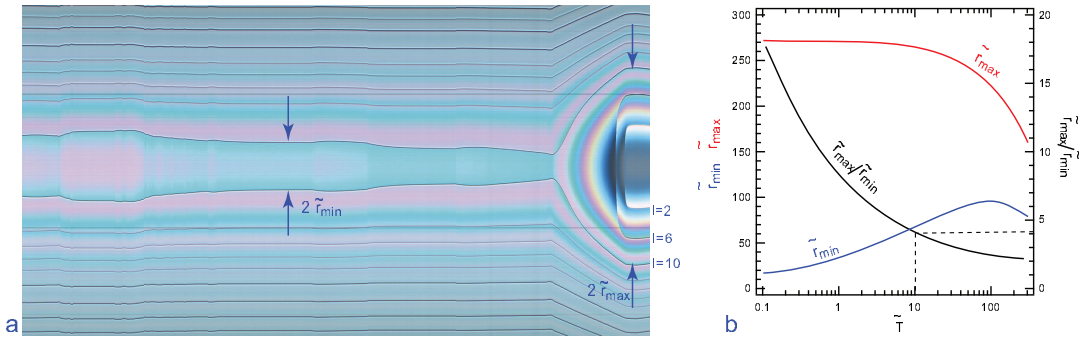

Figure 14. Determination of the reduced tension $\tilde{T}$ from measurement of the stability range of the I=10 DL loop. a) Spatiotemporal cross section extracted from a video. r_{max} and r_{rmin} are the maximal and minimal stable radii of the I=10 loop. c) Plots of $\tilde{r}_{min}$, $\tilde{r}_{max}$ and $\tilde{r}_{max}/\tilde{r}_{min}$ calculated numerically from equation 26 using $\tilde{D} = 290000\mu m$. With $r_{max}/r_{rmin} = 4.1$ determined in (a), one obtains $\tilde{T} \approx 10$.

8.2.3. How large is the tension of the double line with the index I=10?

This critical value of the dimensionless tension $\tilde{T} = 3{\cdot}10^{-3}$ that would be necessary for the thermally excited homogeneous nucleation is much smaller than the one, $\tilde{T} = 10$ that we used in the discussion of the stability of dislocation loops in section 8.2.1. This order of magnitude was in fact inferred from experimental facts reported below.

Let us consider first the Figure 14b which shows variations of $\tilde{r}_{min}$, $\tilde{r}_{max}$ and of the ratio $\tilde{r}_{max}/\tilde{r}_{min}$ calculated numerically as functions of $\tilde{T}$ for the loop I=10. The monotonic variation of the ratio $\tilde{r}_{max}/\tilde{r}_{min}$ with the tension $\tilde{T}$ allows to determine the tension of the I=10 dislocations from measurements of its minimal and maximal radii.

For this purpose we recorded a video showing modifications of the size of the I=10 loop during slow variations of the minimal gap thickness h_{min}. Figure 14a shows the spatio-temporal section extracted from this video. The maximal radius of the I=10 loop on this picture is $r_{max} = 688$ pixels. By means of small and slow variations of h_{min} we also determined the minimal stable radius of the loop $r_{min} \approx 168$ pixels. The ratio r_{max}/r_{min} determined by this means is thus 4.1 which corresponds to $\tilde{T} = 10$ in the plot of Figure 14b.

In conclusion, the thermally triggered nucleation of the I=10 dislocation loop is not plausible because its tension $\tilde{T}$ is much larger than $3 \cdot 10^{-3}$.

Remark: The insert in Figure 13c shows that if the value of $\tilde{T} = 3 \cdot 10^{-3}$ was used in calculations, the minimal stable radius $\tilde{r}_{min}$ would be of the order of 5 so that with $\tilde{r}_{max} \approx 269$ (see Figure 13) the ratio $\tilde{r}_{max}/\tilde{r}_{min}$ would be of the order of 54.

Once the possibility of the homogeneous (i.e. thermally triggered) nucleation is eliminated we have to consider the heterogenous nucleation.

8.3. Nucleation of SL loops on the pair of ±1/2 surface defects

In the light of the recent experiments of Long et al.[11] we can ask what would be the critical compression ratio for nucleation SL loops on a pair of the ±1/2 surface defects separated by the distance w. From considerations in section 2.2 we know that the Frank-Reed mechanism involves the energy barrier corresponding to the critical radius of the dislocation loop $r = w/2$.

Let us suppose that the nucleation defect visible in Figure 6d-1s is similar to the pair of the ±1/2 surface defects. Its radius is $r_d \approx 15\mu m$. Knowing that $p_o = 10\mu m$

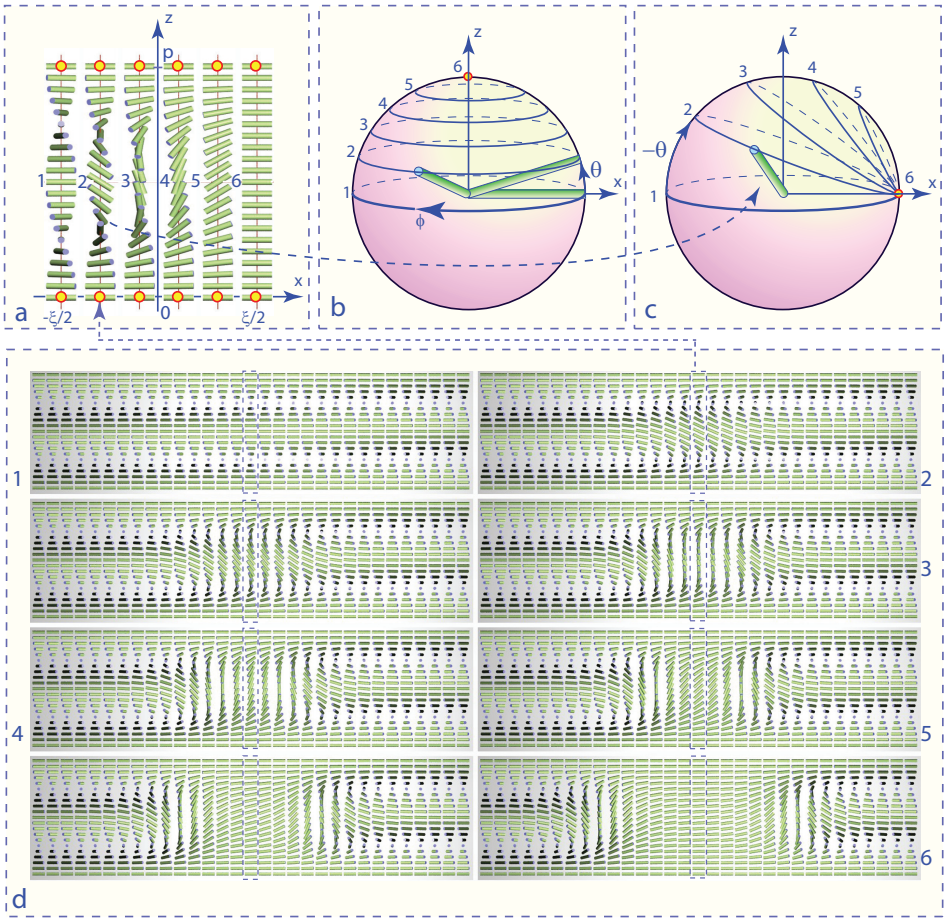

Figure 15. Crude simulation of nucleation of a double dislocation loop. a) Non singular director field $\vec{n}(x,z)$ of a double dislocation (parallel to the y axis and located at z=p/2) obtained by mapping from the degeneracy space of the uniaxial order parameter (North hemisphere) onto the rectangular real space domain $-\xi/2 < x < \xi/2$, $0 < z < p$. The field $\vec{n}(x,z)$ is generated by three successive rotations applied to the vector (1,0,0). b) Rotation by the angle θ around the y axis followed by rotation by the angle ϕ around the z axis. c) Rotation by the angle $-\theta$ around the y axis. d) Simulation of nucleation of a double dislocation loop.

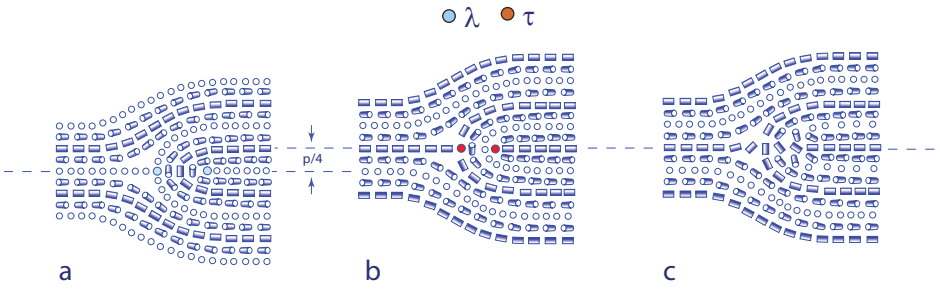

Figure 16. Comparison of director fields in Figure 15 with models of double dislocations proposed by Kleman and Friedel [12]. a) Non singular Kleman-Friedel model. b) Kleman-Friedel model containing a pair of disclinations $\tau_{+1/2}$ and $\tau_{-1/2}$. c) Alternative non singular version of the field shown in (b).

in this experiment, we have $\tilde{r}_d \approx 1.5$. From the Figure 7 we know that the critical compression ratio in this experiment is $CCR = 2.2$. Using equation 29 we obtain $\tilde{T}_{SL} \approx \tilde{r}_d * (CCR - 1) = 1.5 * 1.2 = 1.8$. As we will have seen above in section 8.2.3, the value of the reduced tension of dislocations can be estimated from measurements of their maximal and minimal radii r_{min} and r_{max}. In the case of the double dislocation discussed in section 8.2.3 we obtained the estimate $\tilde{T}_{DL} \approx 10$, five times larger than $\tilde{T}_{SL} = 1.8$.

These two results, $\tilde{T}_{DL} \approx 10$ and $\tilde{T}_{SL} = 1.8$ cannot be compared directly because they were obtained with samples having different pitches. We intend to perform additional experiments allowing to measure $\tilde{T}_{DL}$ and $\tilde{T}_{SL}$ in the same sample.

8.4. Generation of a double dislocation by a continuous deformation of the twisted director field

As already mentioned in section 7, nucleation of double line loops with the Burgers vector of length p was observed in experiments much more frequently than that of single line loops with the Burgers vector $p/2$. At first sight, this fact seems to contradict expectations resulting from studies of dislocations in crystalline solids where the elastic energy per unit length of dislocations grows with the length b of the Burgers vector as b^2.

Explanation of this apparent paradox involves the fundamental topological difference between the single and double dislocation lines that was emphasized by Kleman and Friedel [12] in their seminal article (see Figures 4e and f): the director field of single dislocation lines contains always a singular core while that of double dislocation lines can be non singular for topological reasons. The absence of the singular core in double dislocation lines has two consequences:

(1) their director field is continuous everywhere
(2) they can be generated (or suppressed) by a continuous deformation of the cholesteric helix

An example of such a deformation leading to generation of a double dislocation loop is illustrated in eight pictures of Figure 15d.

To explain how these pictures were generated let us consider first the generation of one DL dislocation parallel to the y axis and located at x=0, z=p/2. Its director field $\vec{n}(x,z)$ shown in Figure 15a was obtained by three successive rotations applied to the director n=(1,0,0):

$$\vec{n}(x,z) = \hat{R}_1^{-1} * \hat{R}_2 * \hat{R}_1 * (1,0,0) \tag{32}$$

where $\hat{R}_1$ is rotation around the y axis by the angle θ (see Figure 15b)

$$\theta = (\pi/8) * (tanh(x/\xi + 1) * (tanh(z/\zeta) - tanh((z-p)/\zeta)) \tag{33}$$

$\hat{R}_2$ is rotation around the y axis by the angle $\phi = \pi z/p$ (see Figure 15b) and $\hat{R}_1^{-1}$ is the rotation inverse to $\hat{R}_1$.

The eight pictures of Figure 15d were obtained in same manner with this difference that not one but two parallel dislocation lines were generated at the same time.

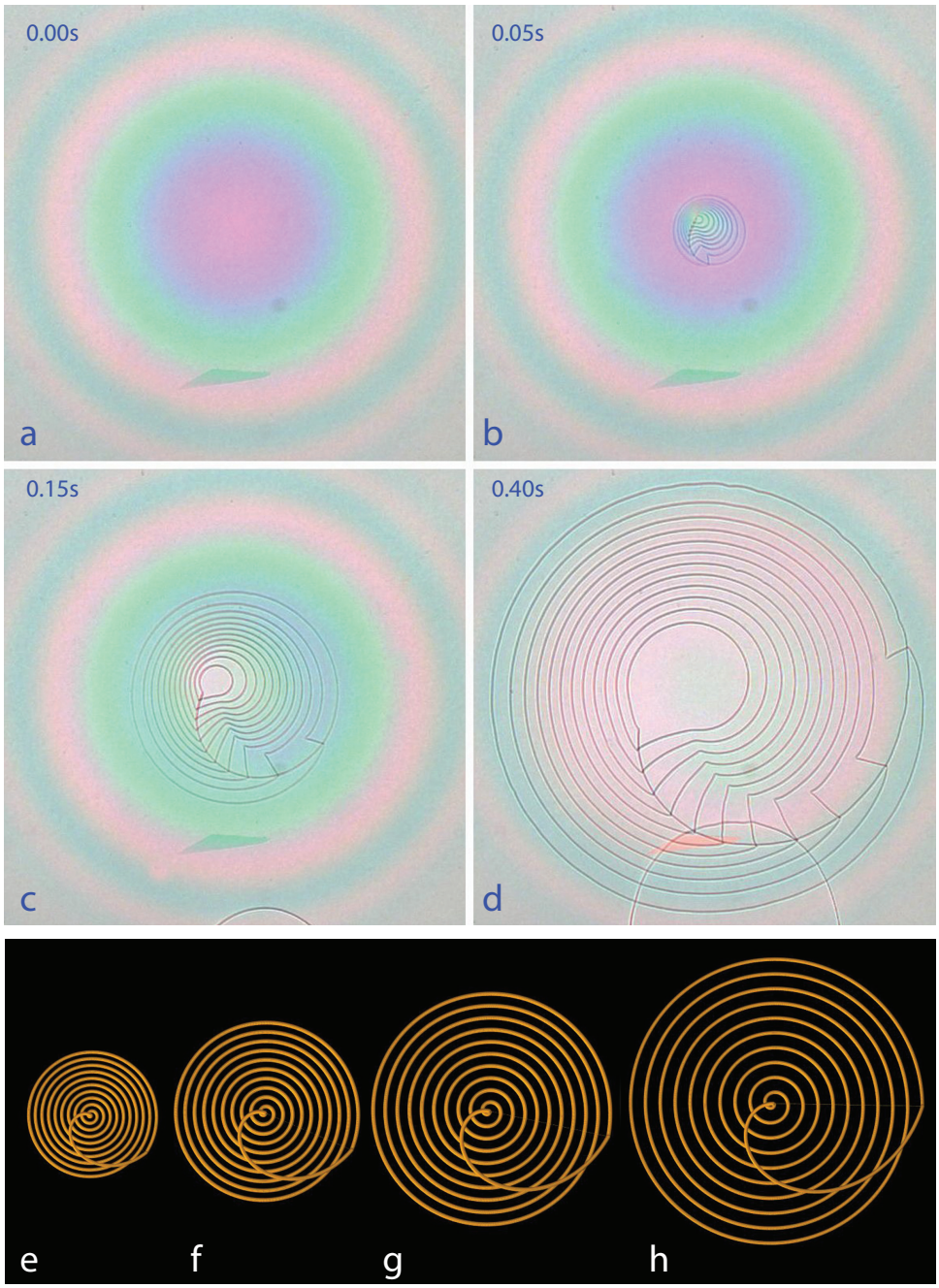

Figure 17. Spiral-shaped double line folded superloop. a-b) Nucleation on an invisible imperfection located on the lower mica sheet. The critical compression ratio of this nucleation event was $CCR = 3.6$. b-d) Expansion driven by the Peach-Koehler force. e-h) Crude simulation of the expanding loop. From topological point of view it is a toroidal coiled unknot $U_{12,1}$.

8.5. Nucleation of the folded superloops

In very clean samples (filtered components) with relatively large cholesteric pitches $p_o > 2\mu m$ confined between mica sheets free of visible imperfections, nucleation of the individual double dislocation loops considered in this paper is in fact quite rare. Instead of that, we observed nucleation of series of loops connected into superloops by two-levels crossings.

As an example we show in Figures 17a-d nucleation and expansion of a superloop made of 12 connected double line loops. This nucleation event occurred at the critical compression ratio $CCR = 3.6$ which is about two times larger then the values of CCR of individual nucleations. In samples with a very large pitch $p_o \approx 40\mu m$, CCR can be of the order of 14.

We have found that the number of folds N_f in folded superloops depends on two parameters: the initial thickness N of the cholesteric layer and the critical compression ratio CCR. In the present article we discussed the limit case of nucleation of the individual dislocation loops ($N_f = 0$) occurring when $CCR = h_I/h_c$ is smaller than 2. For larger values of CCR, nucleation of the primary loop on a surface imperfection is followed by nucleation of secondary loops on the kink carried by the primary loop (see Figure 11 in ref.[8]).

We postpone a more detailed report on nucleation of folded superloops to another paper. Here, in the next section we will focus on generation of knots and links by coalescence of the superloops folded once or twice.

9. Genesis of links and knots by coalescence of folded unknots

9.1. Conjecture on shapes of links and knots confined between the cylindrical mica sheets

From topological point of view, detailed shapes of knots and links do not matter. On the contrary, shapes of real physical knots made of disclinations or dislocations are determined by the elastic and viscous interactions. The case of links and knots made of dislocations in cholesteric layers confined between the cylindrical mica sheets was considered for the first time in ref.[8] where we formulated the conjecture illustrated here in Figure 18. The equilibrium shapes represented in Figures 18b-f are composed of coaxial circular loops interconnected by radial crossings. The circular loops and the radial crossings delimit fields with well defined numbers N of the cholesteric pitches.

The radii of the circular loops depend on the minimal thickness in agreement with considerations in section 5.

9.2. Coalescence of superloops folded once

Collisions between folded superloops nucleated and expanding simultaneously are leading to the coalescence-rewiring processes such as the one represented schematically in Introduction in Figure 1 where the Hopf link was generated by coalescence of two superloops folded once. Below, in Figure 19 we show the same process occurring in a sample with a smaller pitch $p_o \approx 2\mu m$. At this stage of the discussion, it is important to stress that in order to generate the Hopf link, the crossings in the two coalescing folded superloops should have the same sign in terms of the convention used in the theory of knots (see f.ex. ref. [18]). In Figures 1 and 19 this sign the same : "-" . It is easy to check that if the two crossings had different signs, the collision-coalescence

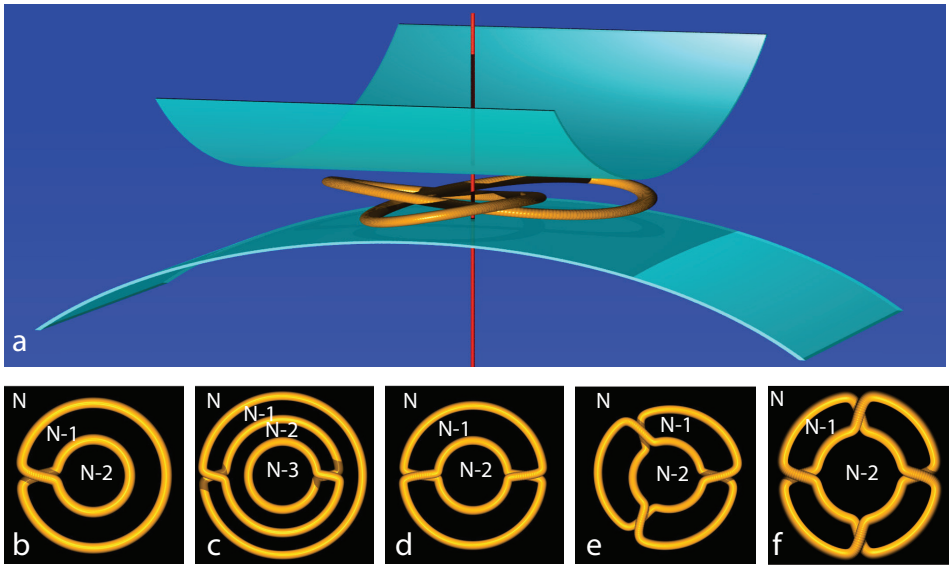

Figure 18. The recent conjecture on shapes of unknots, knots and links flattened physically by the confinement in the crossed cylinders wedge [8]. N labels the number of cholesteric pitches in fields delimited by dislocation lines. a) Perspective view of the confinement of the trefoil knot between the two crossed cylindrical surfaces. b) The shape imposed by the confinement of the unknot folded once. c) The same for the unknot folded twice. d) The same for the Hopf link. e) The same for the trefoil knot. f) The same for the Solomon link.

process would produce two disjoined trivial loops. **Remark:** The cholesteric helix in the 5CB/15CB mixtures is dextrogyre. For this reason, the primary loop nucleated by the compressive strain has the dextrogyre helical shape and is buckled with the kink [15]. During expansion of such primary loop, the secondary loop is nucleated on the kink and one obtains a superloop with one fold connected to the primary loop by the crossing with the sign "-" (see Figures 19i and 19j).

In the experiment depicted in Figure 19 nucleation of the folded loops occurred on very small surface imperfections invisible in microscope. We arrived at this conclusion because when this experiment is repeated several times, nucleation of the two folded loops occurs in the same (x,y) positions.

What kinds of surface defects could be used for a well controlled manner for the genesis of the folded superloops? This is the most challenging issue that we intend to solve in future. If the method of preparation of adequate surface defects was known, it would be possible to generate a larger variety of knots and links. As an example we show in Figure 20 knots and links obtained by coalescence of n_{f1} superloops folded once. All of them belong to the class of torus knots and links. With n_{f1} odd, one obtains torus knots while with n_{f1} even, one gets torus links.

9.3. Coalescence of superloops folded twice

One can also ask what kind of knots and links could be obtained by coalescence of superloops folded twice or more. The case of the coalescence of two superloops folded twice is analysed theoretically in Figure 21. Here, from topological point of view, the first coalescence-rewiring process $AB + CD \Rightarrow AC + BD$ gathers two (folded) unknots from Figure 21a into one (multiply folded) unknot in Figure 21b. The second coalescence-rewiring process $EF + GH \Rightarrow EG + FH$ transform the unknot into the

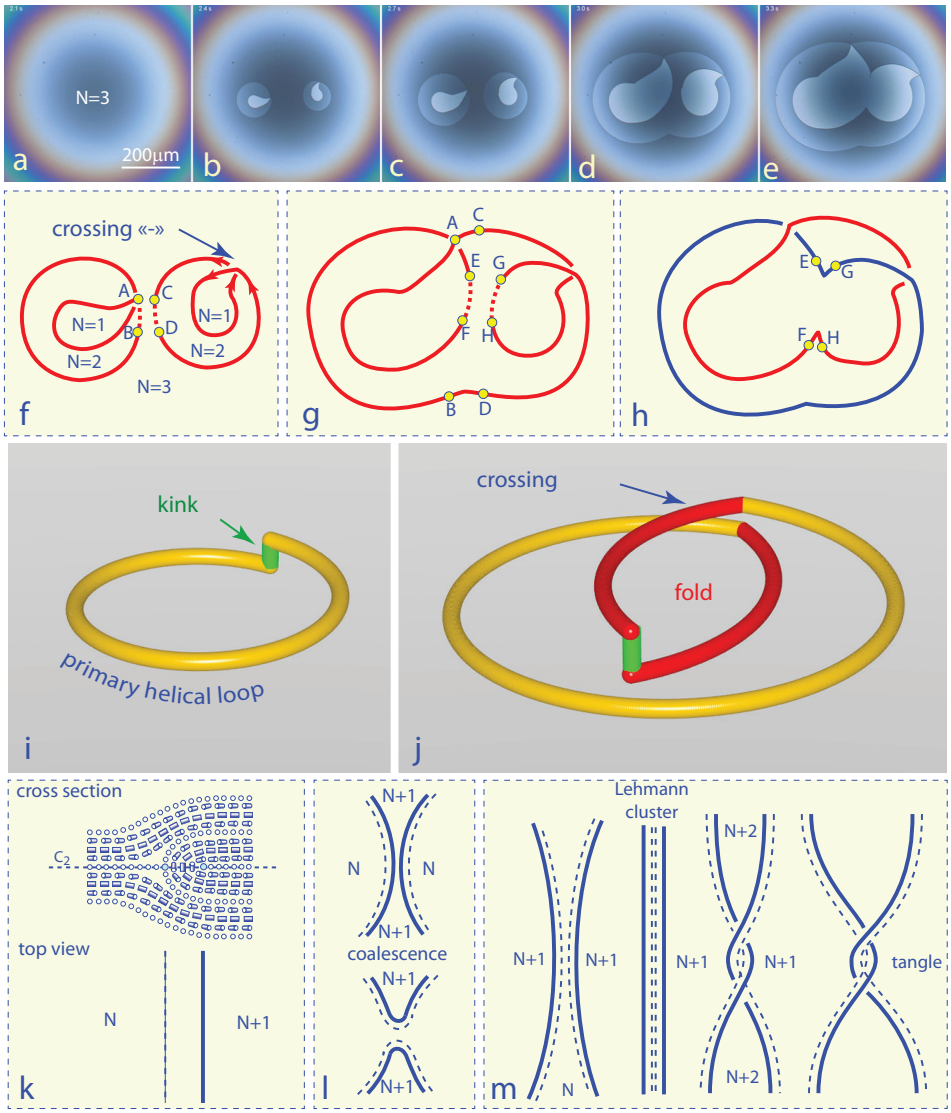

Figure 19. Generation of the Hopf link by coalescence of two unknots folded once. a-b) Simultaneous nucleation of two superloops folded once. b-e) Expansion of the two superloops leading to two successive collision-rewiring events ($p_o \approx 2\mu m$). f-g) Schematic representation of the first $AB + CD \Rightarrow AC + BD$ rewiring. The two superloops coalesce into one superloop with two folds. g-h) Schematic representation of the second $EF + GH \Rightarrow EG + FH$ rewiring. Coalescence of the two folds results in generation of the Hopf link. i) Dextrogyre helical shape of the primary loop buckled with a kink. j) Fold nucleated on the kink during expansion of the primary loop. The sign of the crossing connecting the fold to the primary loop is "-". k) Cross section: symmetry C_2 of the double dislocation with the Burgers vector $b = p$. Top view: the difference between the left and right sides of the dislocations is represented graphically by the dashed and full lines. l) During the collision of two expanding dislocation loops, the contact between their full line sides leads to the rewiring. m) During the collision of two expanding dislocation antiloops (N+1 pitches inside, N pitches outside), the contact between their dashed line sides leads to first to formation of the Lehmann cluster. Under a strong enough tensile strain, the overlapping transition occurs and tangles are generated [9].

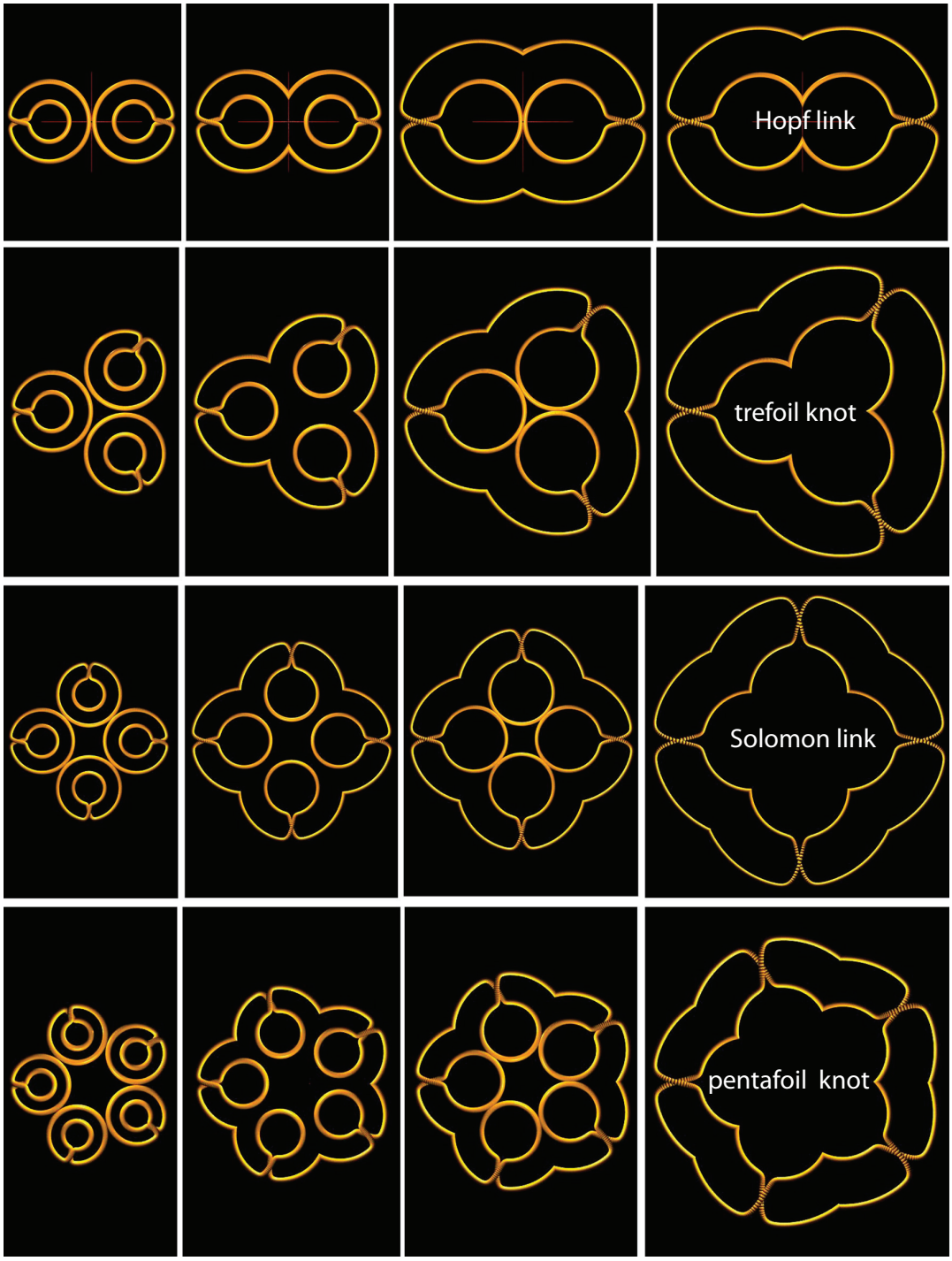

Figure 20. Results of the coalescence of n_{f1} folded unknots: for n_{f1} odd one obtains knots while for n_{f1} even one gets links.

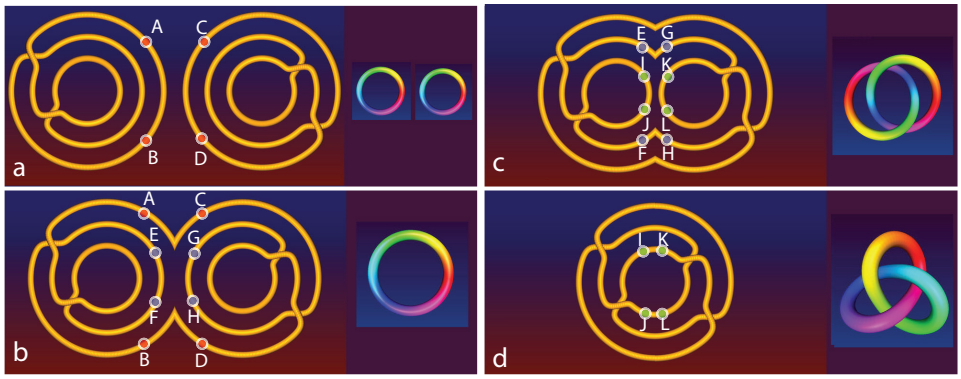

Figure 21. Generation of the trefoil knot by coalescence of two unknots folded twice. a) Two unknots folded twice nucleated simultaneously. a-b) By the coalescence-rewiring of the external segments of the two folded unknots, $AB + CD \Rightarrow AC + BD$ one obtains an unknot folded four times. b-c) By the coalescence-rewiring process $EF + GH \Rightarrow EG + FH$ one obtains the Hopf link with two folds. c-d) By the coalescence-rewiring process $IJ + KL \Rightarrow IK + JL$ one obtains the knot with four crossings which topologically is equivalent to the trefoil knot.

Hopf link (see Figure 21c). The third coalescence-rewiring process $IL+KL \Rightarrow IK+JL$ transforms the Hopf link into the knot with four crossings of the same sign which is equivalent to the trefoil knot (see Figure 22b).

Experimental generation of the trefoil knot by coalescence of two unknots folded twice depicted in Figure 22a is more complex. Here, after nucleation of two unknots folded twice labeled $U_{3,1}$, two other unknots folded once labeled $U_{2,1}$ are nucleated too. In spite of this perturbation, after the collapse of small loops inside the dashed circles, one obtains finally the knot with four crossings of the same sign. Figure 22b shows that the "untwist" Reidemeister move (transformation conserving the topology of the knot) applied to this knot with four crossings suppresses the crossing 3 and one obtains the classical conformation of the trefoil knot with three crossing.

10. Decay of knots and links

10.1. Stability of the crossings

We have pointed above that knots and links can be generated by coalescence of folded unknots. This mechanism can be seen as gathering together the crossings belonging previously to the unknots.

Are these knots and links made of dislocations in cholesterics stable? To answer this question we have to examine in more details the structure and the stability of their Achilles' heels - the radial connections between the coaxial circular loops. Each of these connections is made of dislocations pairs with the total Burgers vector $b = 0$ and some energy per unit length T_{pair} such as the one shown in Figure 23a. Here, the tension T_{pair} is balanced at the crossing point by the tensions T of the dislocations 1 and 2. Knowing the angle $\alpha_{12} \approx 45°$ one obtains $T_{pair} \approx 1.85T$.

Due to the fact that the z position of edge dislocations in equilibrium depends on their orientations (see ref. [15]), the dislocations 1 and 2 are located at different levels

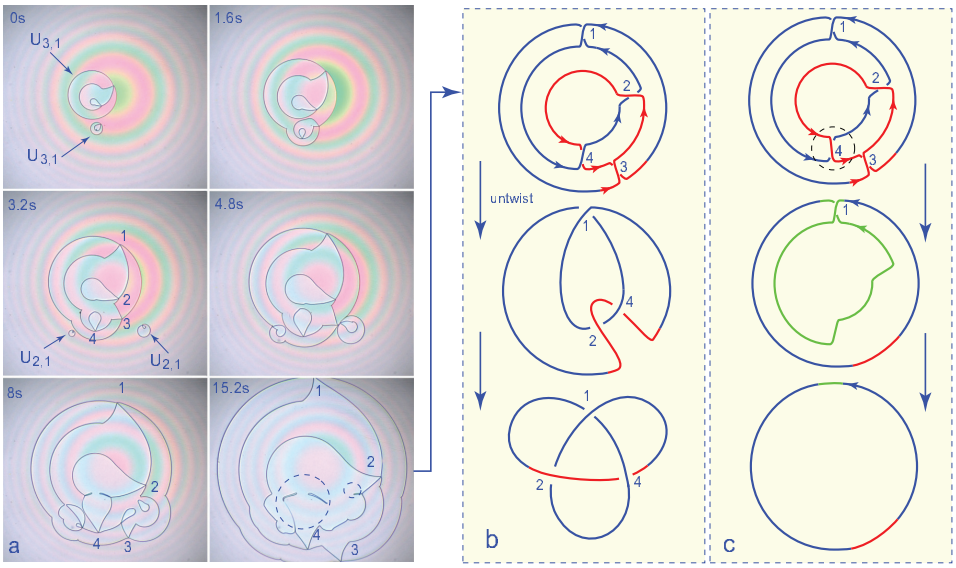

Figure 22. Experimental generation of the trefoil knot by coalescence of folded unknots. a) Generation of a knot with four crossings by coalescence of two folded unknots $U_{3,1}$ nucleated and expanding in the cholesteric layer submitted to a compressive strain (sample with the equilibrium pitch $p_o = 40\mu m$). Let us emphasize that the all four crossings have the same sign "-". b) The Reidemeister move "untwist" applied by thought to the red segment suppresses the crossing 3 and transforms the knot with four crossings into the classical conformation of the trefoil knot with three crossings. c) If the crossing 4 had the sign + instead of -, the knot with four crossings would be equivalent to the trivial unknot $U_{1,1}$.

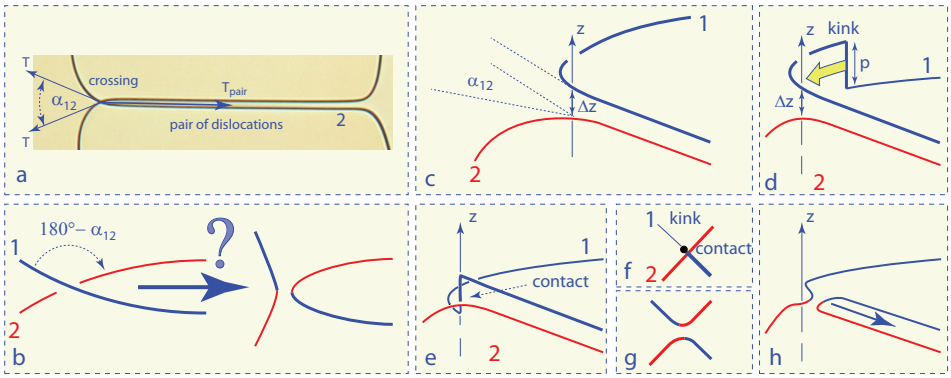

Figure 23. Breaking of a pair of dislocations by reconnection of its crossing. a) Top view, picture taken with a microscope. b) Schematic perspective view of the crossing. c) Perspective view of the same crossing with a kink located on the dislocation 1. d) The kink moving in the direction of dislocation 2. e) The kink in contact with the dislocation 2. e-g) Rewiring of the contact crossing. h) Result of the rewiring of the crossing: the dislocation pair is broken and it retracts.

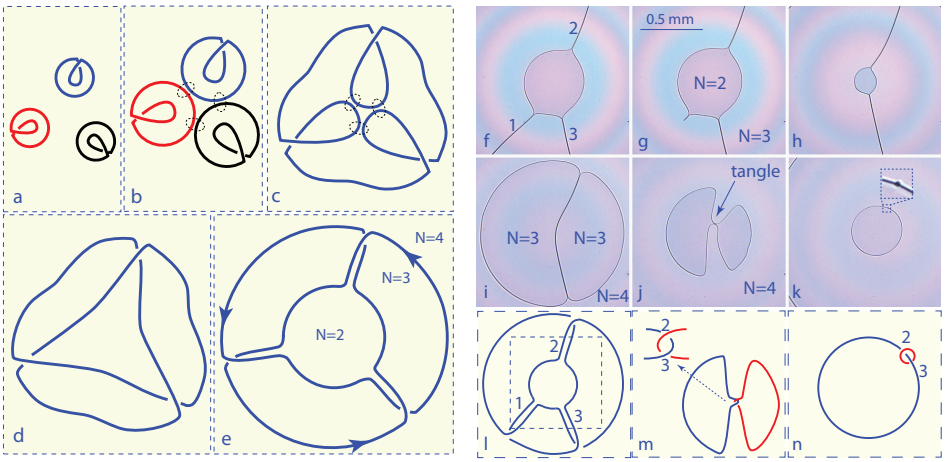

Figure 24. The trefoil knot and its decay into the Hopf link. a-e) Generation of the trefoil knot by coalescence of three unknots folded once. f-k) Observation of the transformation of the trefoil knot into the Hopf link by the non Reidemeister move: breaking of the crossed dislocation pair "1". l-n) Schematic representation of the transformation of the trefoil knot into the Hopf link. n) The necklace configuration of a minimal loop tethered on the cargo loop.

z_1 and z_2 (see Figure 23c) such that

$$\Delta z = z_1 - z_2 = p_o \frac{180^\circ - \alpha_{12}}{360^\circ} \tag{34}$$

In this situation, the crossing seems to be stable (immune against the rewiring) but in fact it has a lethal enemy: kinks of the height p such as the one located on the dislocation 1 in the vicinity of the crossing as shown in Figure 23d. As this kink is mobile, it can come to the crossing and collide with the dislocation 2 (see Figure 23e). This collision leads to the rewiring of the crossing shown in Figures 23f, g and h. After this event, the broken dislocation pair contracts. **Remark:** From topological point of view, the dislocation pair can be broken because its total Burgers vector is $b = 0$. Below we will see how the trefoil knot is transformed into the Hopf link by breaking of one of its three dislocation pairs.

10.2. Decay of the trefoil knot into the Hopf necklace

In the experiment depicted in Figure 24 two remarkable events occurred. The series of five pictures (Figures 24a-e) represents schematically generation of the trefoil knot by coalescence of three unknots folded once. The next six pictures (Figures 24f-k) show the transformation of the trefoil knot into the Hopf link. The first picture in Figure 24f shows the central part of the trefoil knot corresponding to the dashed square area in the scheme of Figure 24l. The next picture shows retractation of the broken dislocation pair 1. The next two pictures (Figures 24h-i) show the shrinking and collapse of the field labeled N=3 due to an increase of the gap thickness. In Figure 24i, the two fields N=3 are separated by the dislocation pair resulting from the connection of pairs 2 and 3.

As the crossings 2 and 3 located at extremities of this unique dislocation pair have the same sign inherited from the trefoil knot, we have to deal with the Hopf link in

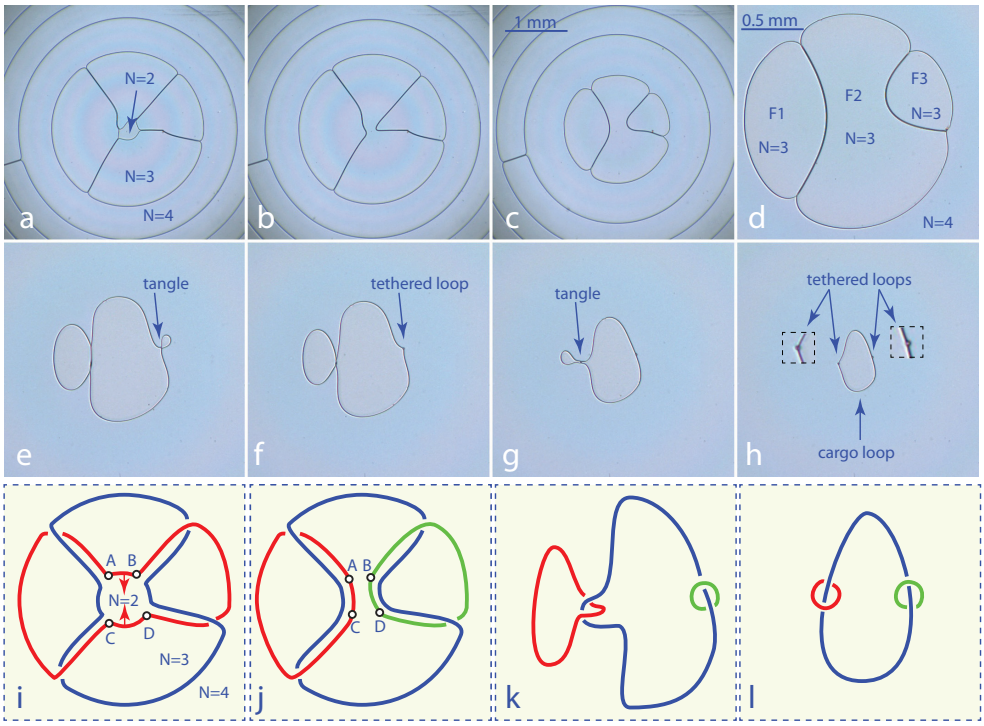

Figure 25. Solomon link and its decay into the Hopf necklace. a-h) Observation in a microscope. i-l) Schematic representation of the transformation.

an unusual configuration. Upon a further increase of the gap thickness, the fields N=2 shrink and a tangle defined in ref.[9] is formed as shown in Figures 24j and m.

The subsequent evolution of this Hopf link is remarkable. One of the dislocation loops forming the Hopf link shrinks until it reaches its minimal stable size. The configuration of the **minimal loop** threaded on the **cargo loop** is the hallmark of the cholesteric order parameter [4]. We propose to call it **the Hopf necklace**. As we will see in the next section a double Hopf necklace results from the decay of the Solomon link. Its structure will be discussed in more details in the forthcoming paper in memory of Gerard Toulouse.

10.3. Decay of the Solomon link to the double Hopf necklace

The Solomon link shown in Figures 25a and 25i was obtained by coalescence of four unknots (superloops) folded once. It has the structure conjectured in Figure 18h: two circular loops interconnected by four dislocation pairs with crossings of the same sign. From topological point of view, it is made of two interlaced closed loops drawn with red and blue lines in Figure 25i.

Due to a small increase of the gap thickness, the central field N=2 shrinks and segments AB and CD of the red loop collide. The rewiring $AB + CD \Rightarrow AC + BD$ splits the red loop into the red and green loops interlaced with the blue loops.

In the experiment, this collision-rewiring process leads to the evolution shown in Figures 25b-d. The final configuration in Figure 25d can be seen as made of three N=3 fields, F1, F2 and F3, separated by dislocation pairs. Due to their tension T_{pair} the two dislocation pairs contract until the fields F1 and F3 reach their minimal size.

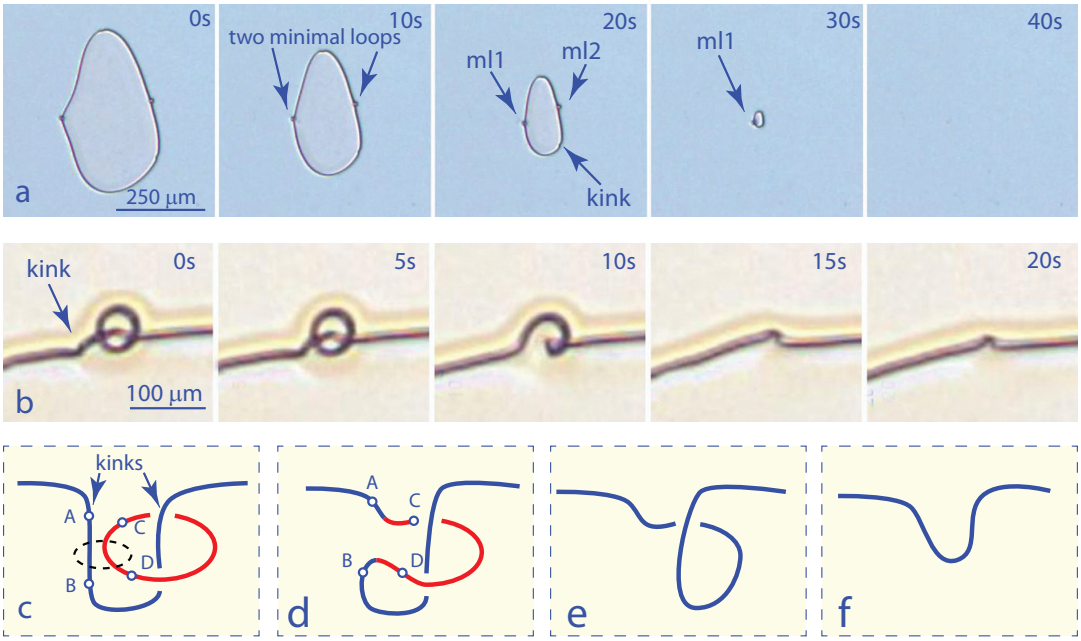

Figure 26. Stability of minimal loops. a) Decay of the double Hopf necklace: 0s-30s - shrinking of the cargo loop, 20s-30s - absorption of the minimal loop ml2 by the cargo loop due to the collision between the minimal loop and the kink ($po \approx 5\mu m$). b) Absorption of the minimal loop by the cargo loop: 0s - kink in the vicinity of the minimal tethered on the cargo loop, 5s-10s collision followed by the rewiring, 10s-20s relaxation of the cargo loop after the absorption of the minimal loop ($po \approx 50\mu m$). c-f) Perspective view of the absorption of the minimal due to its collision with the kink.

The final configuration in Figures 25h and 25i is that of a double Hopf necklace: two minimal loops tethered on one large cargo loop.

10.4. Stability of minimal loops

To start with the discussion of this issue, let us examine the continuation of the experiment represented above in Figure 25 on generation of the Solomon link that evolved into the configuration of the double Hopf necklace. Upon a further increase of the gap thickness, the cargo loop shrinks as it shown in four pictures labeled 0s, 10s, 20s and 30s in Figure 26a. The two minimal loops labeled ml1 and ml2 are well visible in the first three pictures but in the fourth picture (30s) the minimal loop lm2 is missing. The reason of this disappearance is the fatal encounter between the minimal loop ml2 and the kink present on the cargo loop. Result of such an encounter is visualized in the series of five pictures in Figure 26b obtained in another experiment with a sample characterised by a much larger pitch $po \approx 50\mu m$. Clearly, the minimal loop is absorbed by the cargo loop. Details of this encounter are visualized in the series of five schemes in Figures 26c-f. The collision between the kink and the minimal loop leads to the rewiring $AB + CD \Rightarrow AC + BD$ represented in Figures 26c and d.

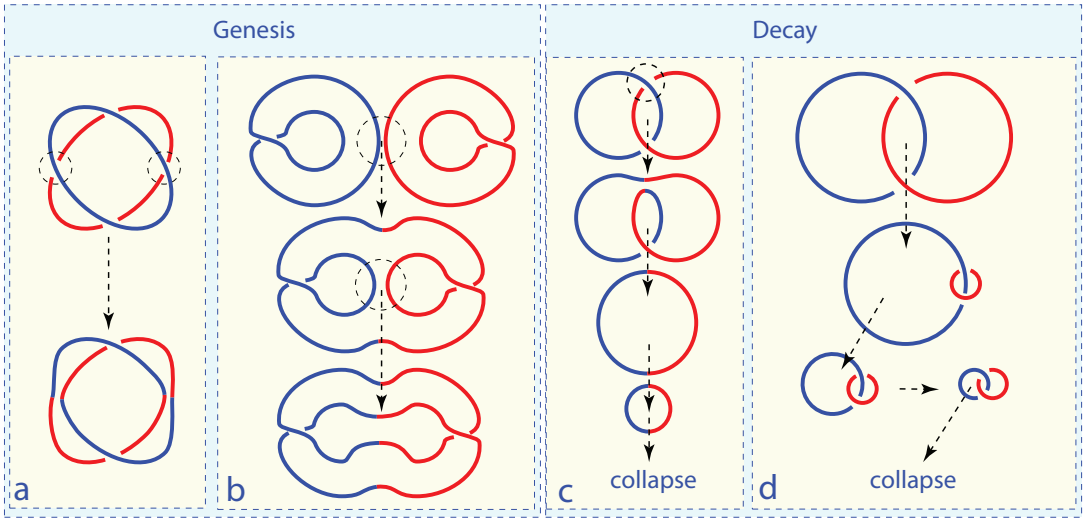

Figure 27. Differences in scenarios of the genesis and decay of knots and links. a) Theoretical genesis of the Hopf link by a frontal collision of two elliptical unknots [20]. Two crossings are rewired. b) The Hopf link in cholesterics is generated by coalescence of two unknots folded once. c) Theoretical decay of the Hopf link [21] involves first its transformation into an unknot by the rewiring of one of its two crossings followed by shrinking and the final collapse of the unknot. d) Decay of the Hopf link in cholesterics starts by its deformation into the Hopf necklace by shrinking of one of the linked loops to its minimal size. The shrunk loop remains tethered on the larger cargo loop. The subsequent shrinking of the cargo loop leads first to the symmetric configuration of linked minimal loops that finally collapse together.

11. Final remarks

11.1. Comparison with the classical schemes of the genesis and decay of knots and links

In this paper we explored experimentally, by optical means, the genesis and decay of knots and links made of dislocations in cholesterics. Do the processes observed is our experiments agree with observations made in other systems and with theoretical schemes obtained by numerical simulations?

Generation and transformations of knots and links by rewiring of crossings have been observed by optical means in two other systems: (1) disclinations in chiral nematic colloids [5], (2) vortices in classical fluids [19]. In the first case, the rewiring of the crossings was driven by local $Nematic \Rightarrow Isotropic \Rightarrow Nematic$ phase transitions driven by heating with a focussed laser beam [5]. In the second case, the rewiring was spontaneous.

Ricca [20] conjectured that knots or links can be also obtained by frontal collisions of vortex unknots of adequate shapes. As an example we show in Figure 27a the genesis of the Hopf link by rewiring of the two crossings of two colliding elliptical unknots. This scheme is different from the genesis of the Hopf links by lateral collision of folded unknots observed in our experiments (see Figure 27b.)

The decay of the Hopf link observed in our experiments (see Figure 27d) is also different from the minimal unlinking pathway proposed by Liu et al. [21] (see Figure 27c). In the theoretical scheme, the decay of the Hopf links involves two steps: (1) transformation of the Hopf link into the unknot by rewiring of one of its two crossings, (2) shrinking and collapse of the unknot. In our experiments, the decay of the Hopf link involves three steps: (1) shrinking of one of the interlaced loops until it reaches its

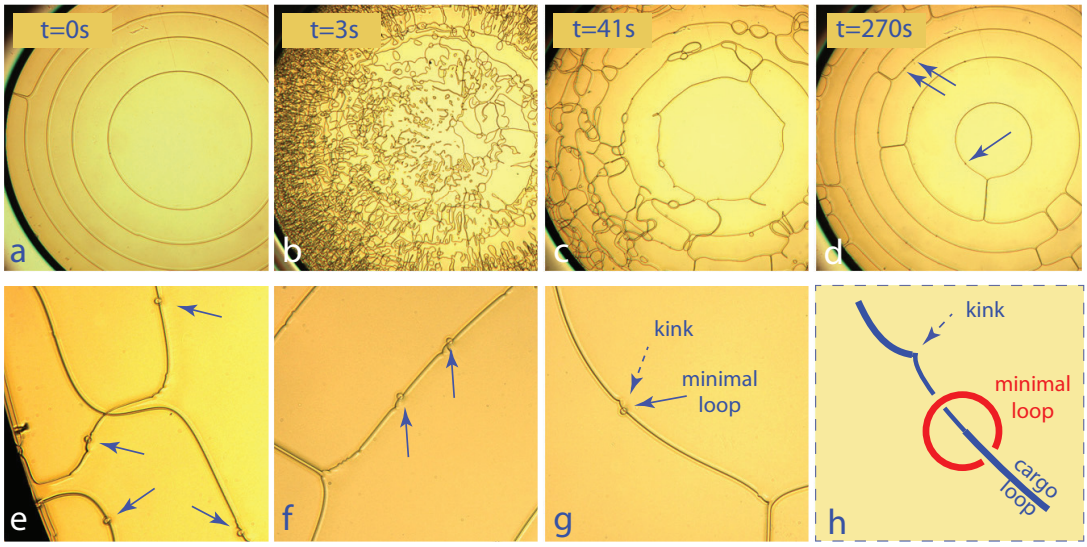

Figure 28. Genesis of a multiple Hopf necklace. a) Initial pattern of loops and superloops. b) Dense tangle of dislocations generated mechanically by rapid and large changes of the gap thickness h_{min}. b-d) Elastic relaxation. d) Arrows indicate three of seventeen minimal loops visible in this picture. e-g) Views of few minimal loops at higher magnification. h) Geometry of the texture in picture g.

minimal size. By this means, the classical Hopf link is transformed into its asymmetric configuration made of a minimal loop tethered on a large cargo loop, (2) shrinking of the cargo loop until it reaches its minimal size, (3) shrinking and the final collapse of the minimal Hopf link as a whole.

11.2. Hopf necklaces

The Hopf necklace, i.e. the asymmetric configuration of the Hopf link made of a minimal loop tethered on a large cargo loop, was observed for the first time by Bouligand [3]. We have seen above that the decay of the Solomon link passes also through the asymmetric configuration which, in this case, is made of two minimal loops tethered on the large cargo loop (see Figures 25d and l). Remarkably, this configuration, that can be called the **double Hopf necklace**, was predicted theoretically by Bouligand et al.[4].

Let us stress that in our experiments with the double dislocation lines, the configuration of **multiple Hopf necklaces** made of several minimal loops tethered on cargo loops turned out to be quite ubiquitous. The reason for which they have been not reported previously is probably the small size of the minimal loops of the order of the cholesteric pitch; in samples with micrometric and submicrometric pitches they can be easily confused with dust particles trapped by dislocations.

We have seen in our experiments that knots and links made of the double dislocations can be generated by two other methods : (1) rapid $Isotropic \Rightarrow Cholesteric$ thermal quench used presumably by Bouligand [3], (2) strong mechanical perturbation of the system of the concentric dislocation loops by flows due to rapid and large changes of the gap thickness h_{min}.

The second method turned out to be very efficient for production of the multiple Hopf necklaces. Indeed, in one of experiments (see Figure 28) we have found 25

minimal loops tethered on multiply folded cargo loops. Production of such multiple Hopf necklaces occurs in two stages. It starts by a strong deformation of the initial loops and superloops convected by complex flows, that could seen as turbulent, accompanied by rapid nucleation of new small folded superloops. After this initial stage that lasts for a few seconds, one obtains a dense and complex texture of folded dislocation loops. As the total length of dislocations in it is multiplied by a factor of order of the order of 100 with respect to the initial length of superloops in equilibrium, this texture relaxes elastically by the collision, rewiring and shrinking processes into the multiple Hopf necklace. The characteristic time of this relaxation depends on the pitch of the cholesteric helix and is of the order of 10 minutes for $p_o \approx 50\mu m$. The relaxation process driven by the decrease in the free energy of the distortion follows a special topological path which remains to be found.

Conflicts of interest

There are no conflicts to declare.

Acknowledgements

One of the authors (P.P) is grateful to C.T. Imrie, R.D. Kamien and O.D. Lavrentovich for the invitation to participate to the memorial issue of Liquid Crystals Reviews in honor of Maurice Kleman. The work on this memorial article [15] triggered experiments on emission of dislocation loops in strained cholesteric layers presented here. We thank also Yves Pomeau and Bernard Derrida for the invitation to participate to the memorial issue of Comptes Rendus de l'Académie des Sciences in honor of Gerard Toulouse. This second memorial article is devoted to "objects with a double topological character" such as knots and links made of topological linear defects.

We address our thanks for the hospitality to Yvan Smalyukh at the "International Institute for Sustainability with Knotted Chiral Metamatter (WPI-SKCM2)".

The new experimental setup tailored for production of cylinder/cylinder mica wedges was inspired by discussions with M. Zeghal and built by V. Klein, J. Sanchez and S. Saranga. We also benefitted from discussions with P. Oswald, Y. Smalyukh, O. Lavrentovich and A. Leforestier as well from the help of I. Settouraman, M. Bottineau, J. Vieira, I. Nimaga and C. Goldmann.

We would like also thank the referee for indication of the recent paper of Long et al. [11] on nucleation of disclination loops in nematics as well as for numerous constructive remarks and queries.

Last but not least, P.P. would like to thank R. Bartolino, R. Barberi and B. Zappone for their warm hospitality during the ECLC2023.

We would like to emphasize that we were introduced to the complexity of knots and links by interactions with P.-G. de Gennes [22] and Piotr Pieranski [23].

This work was financed by FCT-Fundação para a Ciência e a Tecnologia, I.P., in the scope of the projects LA/P/0037/2020, UIDP/50025/2020 and UIDB/50025/2020 of the Associate Laboratory Institute of Nanostructures, Nanomodelling and Nanofabricationi3N. European Cooperation in Science and Technology (COST) Action understanding interaction light - biological surfaces: possibility for new electronic materials and devices (PhoBioS,CA21159).

References

[1] Toulouse G., Kleman M. Principles of a classification of defects in ordered media. Journal de Physique Lettres 1976;37:L-149.

[2] Chaikin P.M., Lubensky T. Principles of condensed matter physics. Cambridge University Press 2012.

[3] Bouligand Y. Recherches sur les textures des états mésomorphes. 6- Dislocations coin et signification des cloisons de Grandjean-Cano dans les cholestériques. Journal de Physique 1974;35:959-981.

[4] Bouligand Y., Derrida B., Ponaru V., Pomeau Y., Toulouse G. Distorsions with double topological character: the case of cholesterics. Journal de Physique 1978;39:863-867.

[5] Tkalec U., Ravnik M., Čopar S., Žumer S., Muševič I. Reconfigurable knots and links in chiral nematic colloids. Science 2011;333:62-65.

[6] Seč D., Čopar S., Žumer S. Topological zoo of free-standing knots in confined chiral nematic fluids. Nature Communications 2014;5:1-7.

[7] Smalyukh I. Review: knots and other new topological effects in liquid crystals and colloids. Rep. Prog. Phys. 2020;83:1-46.

[8] Pieranski P. and Godinho M.H. Fertile metastability. Liquid Crystals 2023;50:1177-1192.

[9] Pieranski P., Zeghal M., Godinho M.H., Judeinstein P., Bouffet-Klein R., Liagre B., Rouger N. Topological metadefects: tangles of dislocations. Phys. Rev. Lett. 2023;131:128101-1–128101-5.

[10] Friedel J. and de Gennes P.-G. Boucles de disinclinaisons dans les cristaux liquides. Comptes Rendus Ac. Sc. 1969;268:B 257–259.

[11] Long C., Deutsch M.G., Angelo J., Culbreath C., Yokoyama H., Selinger J.V., Selinger R.L.B. Frank-Reed mechanism in nematic liquid crystals. Phys. Rev. X. 2024;14:011044-1–011044-11.

[12] Kleman M., Friedel J. Lignes de dislocations dans les cholestériques. J. de Physique. 1969;30:555–654.

[13] Zappone B. and Bartolino R. Topological barriers to defect nucleation generate large mechanical forces in an ordered fluid. PNAS 2021;118:44.

[14] Long C., Selinger, J. V. Applications of the Peach-Koehler force in liquid crystals. Liquid Crystals 2024; 117. doi: 10.1080/02678292.2023.2294957.

[15] Pieranski P., Cholesteric dislocations in mica wedges. Liq. Cryst. Rev. 2022;10:6-33.

[16] Angelo J., Culbreath C., Yokoyama C. Breaking planar liquid crystal anchoring to form controllable twist disclination loops. Molecular Crystals and Liquid Crystals 2017;646:214-219.

[17] Kurik M., Lavrentovich O. Defects in liquid crystals: homotopy and experimental studies. Usp. Fiz. Nauk 1988;154:381-431.

[18] Pieranski Piotr, Baranska J, Skjetorp A. Tendril perversiona physical implication of the topological conservation law. Eur. J. Physics 2004;25:613–621.

[19] Kleckner D. and Irvine T.M. Creation and dynamics of knotted vortices. Nature Physics 2013;9:253–258.

[20] Ricca R.L. New developpements in topological fluid mechanics. Il Nouovo Cimento 2009;32:185–192.

[21] Liu X., Ricca R.L., Li X. Minimal unlinking pathways as geodesics in knot polynomial space. Communications Physics 2020;3:136.

[22] de Gennes P.-G., Tight knots. Macromolecules 1984;17:703.

[23] Pieranski Piotr, "In search of ideal Knots" in "Ideal knots" edited by A. Stasiak, V. Katritch and L.H. Kaufman, World Scientific 1998.